JGR Solid Earth

RESEARCH ARTICLE
10.1029/2021JB023715

Thermal Regime of Slow and Ultraslow Spreading Ridges Controlled by Melt Supply and Modes of Emplacement

Jie Chen[1,2], Jean-Arthur Olive[3], and Mathilde Cannat[1]

[1]Institut de physique du globe de Paris, Université Paris Cité, CNRS, Paris, France, [2]Now at Key Laboratory of Submarine Geosciences, Second Institute of Oceanography, MNR, Hangzhou, China, [3]Laboratoire de Géologie, CNRS - Ecole Normale Supérieure, PSL University, Paris, France

Abstract Melt supply at slow-ultraslow spreading ridges is overall reduced and highly variable. Magma cooling and crystallization substantially shape the axial thermal regime by providing heat that is lost to the ocean through conduction and hydrothermal convection. Geological data suggest that melt is emplaced over a wide depth range, variably accessible to hydrothermal cooling, and that periods of higher and lower melt supply may alternate at a given location. Until now, numerical models focused on steady-state thermal regimes controlled by either spreading rate or melt supply, falling short at slow-ultraslow ridges. Here we present results from a 2-D numerical thermal model that couples repeated melt injections and hydrothermal convection. We first constrain thermal regimes inferred from two ultraslow-spreading endmembers in melt supply at the Southwest Indian Ridge (SWIR): a magmatically robust endmember at 50°28'E and a nearly amagmatic endmember at 64°30'E. We adjust parameters associated with melt supply (the melt injection frequency and the temperature of the host rocks upon melt emplacement) and hydrothermal circulation (the extent and permeability of the hydrothermal system). Our simulations predict that greater melt injection frequencies unsurprisingly produce hotter thermal regimes. However, at a given frequency, melt emplacement in cooler host rocks (e.g., <800°C) causes cooler thermal regimes with transient black smoker-type hydrothermal circulation that extracts heat efficiently. Periodic waxing and waning magma supply, as proposed from geological data at the SWIR 50°28'E, induces an oscillatory thermal regime. Transience in the axial thermo-mechanical state may be an integral part of lower-crustal construction at magmatically robust sections of slow-ultraslow ridges.

Plain Language Summary The thermal regime at mid-ocean ridges reflects a dynamic balance between heat supplied by magmatic injections and cooling through hydrothermal convection. Geological observations show that slow and ultraslow spreading ridges have a diverse melt supply, which may be emplaced at a wide range of depths with variable temperatures and over periods of alternating high and low melt supply, increasing the thermal regime variability. Until now, numerical models focused on steady-state thermal regimes controlled by either spreading rate or melt supply, falling short at slow and ultraslow ridges. We use a coupled numerical model that fuels hydrothermal convection with repeated magmatic intrusions. We constrain thermal regimes inferred from two melt-supply endmembers of ultraslow ridges, and then explore the variability of the thermal regime by adjusting parameters associated with melt supply and hydrothermal circulation. Our simulations show that while higher frequencies of melt injections (unsurprisingly) produce hotter thermal regimes, the temperature of the host rock upon melt emplacement exerts a strong control on the geotherm. Melt injections into cold rocks could cause efficient hydrothermal heat removal and a cooler thermal regime. We also investigate how cyclic changes in melt injection frequencies produce an oscillatory thermal regime at a given ridge location.

Key Points:

- Numerical models reveal the sensitivity of slow mid-ocean ridge thermal regimes to magma supply and mode of emplacement
- Temperature of host rock upon melt emplacement exerts a strong control on the thermal regime
- Cyclic changes with waxing and waning phases of melt injection frequencies shape an oscillatory thermal regime at the Southwest Indian Ridge 50°28'E

Supporting Information:

Supporting Information may be found in the online version of this article.

Correspondence to:

J. Chen,
chenjie.geo@outlook.com

Citation:

Chen, J., Olive, J.-A., & Cannat, M. (2022). Thermal regime of slow and ultraslow spreading ridges controlled by melt supply and modes of emplacement. *Journal of Geophysical Research: Solid Earth*, *127*, e2021JB023715. https://doi.org/10.1029/2021JB023715

Received 2 DEC 2021
Accepted 29 MAR 2022

1. Introduction

Melt supply at mid-ocean ridges (MORs), that is, the volume flux of magma ascending from the asthenosphere to the ridge axis to form the oceanic crust is a key control on seafloor spreading modes. Melt plays a dual role in the formation of oceanic lithosphere: repeated magmatic intrusions accommodate a fraction of the plate divergence, and they also alter the thermal regime of the ridge by releasing specific and latent heat upon cooling and crystallizing (Buck et al., 2005; Cannat et al., 2019; Phipps Morgan & Chen, 1993). At slow and ultraslow spreading ridges (full spreading rate of <40 mm/yr), melt supply is highly variable (Chen, 1992; Christeson et al., 2019) due to along-axis melt focusing from segment ends to segment center (Cannat et al., 1995; Lin et al., 1990; Kuo & Forsyth, 1988; Standish et al., 2008). This melt may be emplaced over a wide range of depths,

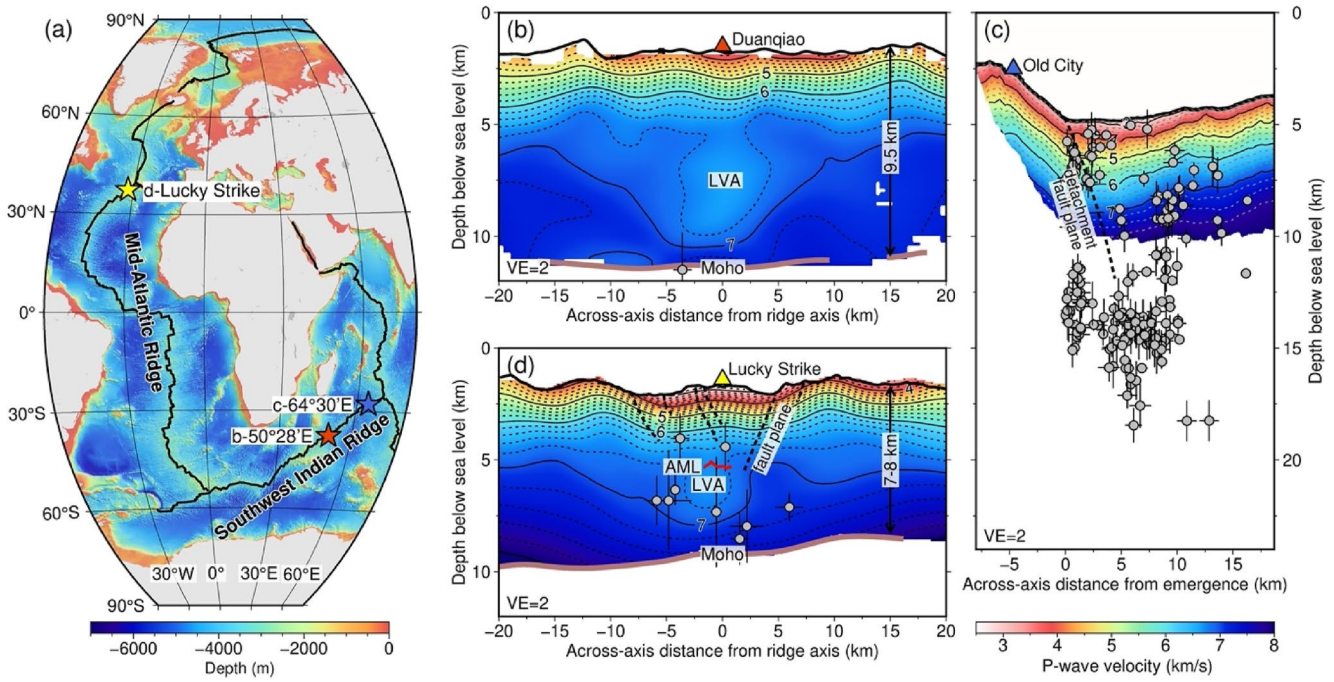

Figure 1. (a) Bathymetric map for the Southwest Indian Ridge (SWIR) and Mid-Atlantic Ridge (MAR). Stars show the locations of the SWIR 50°28'E, SWIR 64°30'E, and MAR Lucky Strike. (b) *P*-wave seismic velocity structure (VE = 2 and the same below) across the ridge axis at the SWIR 50°28'E (Jian et al., 2017). Contours are in 0.2 km/s intervals (the same below). The Moho interface (thick brown lines) is based on PmP arrivals (Jian et al., 2017). Gray circles with error bars are microearthquakes (Yu et al., 2018). The Duanqiao hydrothermal field exposes relict black-smoker chimneys (Chen et al., 2021; Yang et al., 2017). (c) *P*-wave seismic velocity structure across the active detachment fault at the SWIR 64°30'E (Momoh et al., 2017). Detachment fault plane is drawn by seismic reflection (Momoh et al., 2017, 2020). Microearthquakes are from Chen et al. (2020). The Old City hydrothermal field has active low-temperature, carbonate-brucite chimneys. (d) P-wave seismic velocity structure across the ridge axis at the Lucky Strike (Seher et al., 2010). The Moho interface is based on PmP arrivals (Seher et al., 2010). Microearthquakes are from Dusunur et al. (2009). The AML (red line) and normal fault planes (dashed lines) are imaged by seismic reflection (Combier et al., 2015; Singh et al., 2006). The Lucky Strike hydrothermal field has active high-temperature black smokers (Langmuir et al., 1997). LVA, low-velocity anomaly; AML, axial melt lens.

from lava flows on the seafloor to isolated gabbro bodies crystallized from unextracted melt that remains trapped in the mantle (Cannat et al., 1995; Dick, 1989). Cannat et al. (2019) proposed that the variability of melt supply (both in volume flux and depth of emplacement) could result in sharp along-axis transitions in the thermal regime, resulting in dramatic shifts in lithospheric thickness and strength over along-axis distances <30 km, for example, the transition from volcanic to ultramafic seafloor in the eastern part of the ultraslow spreading Southwest Indian Ridge (SWIR in Figure 1a; full spreading rate of ~14 mm/yr). Magmatic heat is extracted to the ocean by hydrothermal circulation, which is enabled by tectonic processes (i.e., faults and fissures providing pathways for hydrothermal fluids), and manifests at the seafloor as clusters of hydrothermal vents (e.g., Lowell et al., 2013). The resulting thermal regime reflects a balance between magmatic heat supply and hydrothermal heat removal (Phipps Morgan & Chen, 1993; Theissen-Krah et al., 2011).

The thermal structure of MOR axes includes two isotherms of interest at 650 and 1,000°C, which should outline regions of brittle deformation and crystal mush zones, respectively (McKenzie et al., 2005; Phipps Morgan & Chen, 1993; Sinton & Detrick, 1992). The maximum depth of earthquakes is believed to be a proxy for the location of the brittle-ductile transition (BDT), roughly corresponding to the 650°C isotherm (Anderson, 1995; McKenzie et al., 2005). Seismically imaged low-velocity anomalies (LVAs) topped by axial melt lens (AML) reflectors can be an additional proxy for persistent crystal mush zones that are enclosed by the basaltic solidus at 1,000°C (Fontaine et al., 2011; Sinton & Detrick, 1992). Thermal models of MOR axes typically predict a colder thermal regime as spreading rate decreases, with the impossibility to sustain long-lived magmatic mush zones at crustal depths at slow and ultraslow MORs (Phipps Morgan & Chen, 1993; Theissen-Krah et al., 2011).

However, several seismic observations appear to contradict this expectation. The thermal regime of the SWIR, for example, is inferred to vary between two magma supply endmembers: a magmatically robust endmember

(e.g., at 50°28'E: Chen et al., 2021) and a nearly amagmatic endmember (e.g., at 64°30'E: Sauter et al., 2013). The center of the 50°28'E segment (Figure 1b) is characterized by a low-velocity mush zone between ∼4 and 9 km below seafloor (BSF) with an along-axis extent of 7–8 km, and its magmatic crustal thickness has remained 9.5 km over the last >3 Myr (Jian et al., 2017). At 64°30'E (Figure 1c), the deepest earthquake lies at ∼15 km (Chen et al., 2020) in a context of nearly zero magmatic crust (Cannat et al., 2006; Momoh et al., 2017; Sauter et al., 2013), and seismic velocity gradients increase almost linearly with depth, which has been interpreted to reflect a decrease in serpentinization and fracturing with depth (Corbalán et al., 2021; Momoh et al., 2017). Surprisingly, the more magmatic detachment system in the "Dragon Horn" section of the SWIR at 49°39'E has the same spreading rate but features earthquakes that occur even deeper than at this nearly amagmatic SWIR 64°30'E section (18 vs. 15 km; Chen et al., 2020; Tao et al., 2020; Yu et al., 2018). Thermal models of slow and ultraslow MORs must therefore account for the possibility of extensive regions of crystal mush at crustal depths, as well as for a possible decorrelation between the depth of the 650°C isotherm and magma supply, at a given spreading rate.

The thermal regime of fast spreading MOR axes is often considered to be near steady-state over geological time, as evidenced by shallow, nearly continuous AMLs (Detrick et al., 1987; Marjanović et al., 2014) and nearly uniform off-axis seafloor morphology (Soule et al., 2009). By contrast, the axial thermal regime at slow and ultraslow spreading ridges appears temporally variable, and cyclic changes in melt supply with alternating waxing and waning phases over a few 100s of kyrs have been documented at a few slow and ultraslow spreading, magmatically robust ridge sections, such as the centers of the SWIR 50°28'E segment (Chen et al., 2021) and the Menez Gwen segment of the Mid-Atlantic Ridge (MAR; Klischies et al., 2019). Cyclic melt supply at the SWIR 50°28'E results in the accretion of smooth domal volcanos during waxing phases and of hummocky ridges during waning phases (Chen et al., 2021). Interestingly, the thickness of the magmatic crust does not appear to vary significantly at these time scales (Jian et al., 2017; Li et al., 2015), which may reflect a damping process characteristic of ultraslow settings (Chen et al., 2021).

Consequently, slow and ultraslow spreading ridges are natural laboratories for identifying key controls on the variability of the axial thermal regime that is documented across sections that spread at similar rates, and for assessing the impact of a transient melt supply on the thermal regime. This paper applies a modified version of a 2D numerical thermal model (Fan et al., 2021) that couples repeated magma intrusions and hydrothermal convection (Figure 2b). The previous version in Fan et al. (2021) focused on simulating the cold thermal regimes of ultraslow spreading ridge sections with low to nearly zero melt supply, but did not consider sections with robust melt supply, where the thermal regimes show especially high sensitivity to melt injection frequencies (e.g., Figure 4 in Fan et al., 2021).

We use the modified model to constrain the thermal regimes of two melt supply endmembers of ultraslow spreading ridges (the most magmatically robust SWIR 50°28'E and the nearly amagmatic SWIR 64°30'E; Figure 1). We then take the SWIR 50°28'E as a reference in our numerical simulations of cyclic changes in melt supply. To do so, we adjust parameters associated with how much and/or at what depth the melt is emplaced, and we vary the impact of hydrothermal circulation by adjusting the maximum depth and the permeability of the hydrothermal domain. To explore the impact of the depth at which melt is emplaced, we periodically intrude melt as a lens centered in the model, whose top coincides with an isotherm. We call this isotherm the magma emplacement temperature. More precisely, it is the temperature of the host rock upon melt emplacement. This allows us to distinguish between repeated intrusions into the cold/shallow and the hot/deep lithosphere. With four groups of simulations (Figure 2) and two important observables in the model, for example, the depths to the BDT (650°C isotherm) and the mush zone (1,000°C isotherm), we successfully account for the thermal regimes of two ultraslow spreading endmembers and for the variability of the thermal regimes at ultraslow (extending to slow) spreading ridges. We also constrain the range of melt injection frequencies, exploring the thermal impact of the cyclic changes of melt supply inferred from geological data at the SWIR 50°28'E.

2. Methods

2.1. Model Setup

We model a two-dimensional section of young oceanic lithosphere through which heat can be transferred conductively, as well as advected by hydrothermal fluids in a shallow, permeable region (Figure 2). We follow the

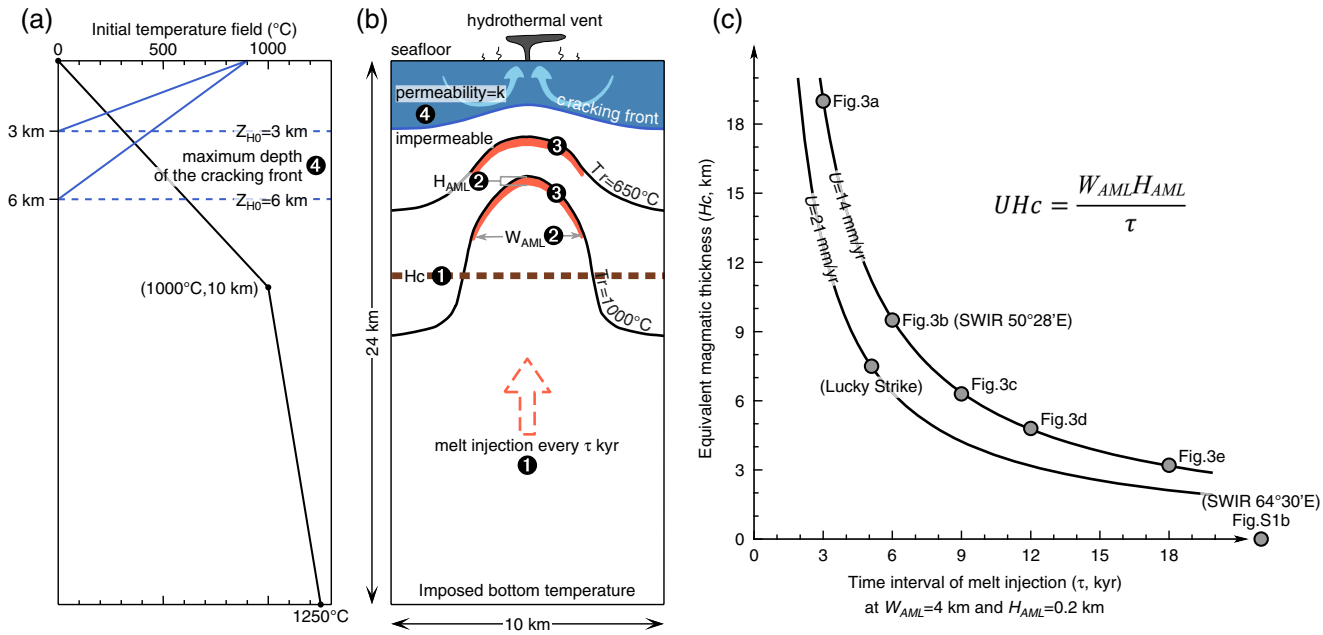

Figure 2. (a) Initial temperature field and the setting of the maximum depth of the cracking front (Z_{H0}). (b) Cartoon of the thermal model setup, modified from Fan et al. (2021). Numerical labels correspond to the four groups of simulations. (c) Equivalent magmatic thickness (Hc) versus time interval of melt injection (τ) at $W_{AML} = 4$ km and $H_{AML} = 0.2$ km, according to Equation 5. W_{AML}, width of AML; H_{AML}, thickness of AML; Tr, temperature of host rock upon melt emplacement; U, full spreading rate.

numerical approach of Fan et al. (2021) and Olive and Crone (2018), who used a finite volume method to solve for conservation of mass and energy in fluid-saturated, non-deforming porous medium obeying Darcy's law:

$$\nabla \cdot \left(-\frac{k}{\mu_f} (\nabla \boldsymbol{P} - \rho_f \boldsymbol{g}) \right) = 0, \tag{1}$$

where k is the permeability of the hydrothermal layer, μ_f is the viscosity of the fluids, and ρ_f is the density of the fluids. The gradient of pressure ($\nabla \boldsymbol{P}$) and the acceleration of gravity ($\boldsymbol{g}$) in bold are vectors. The fluid velocity ($\boldsymbol{v_f}$) corresponds to the term inside the divergence operator. To evolve the temperature field T, we solve Equation 1 with the heat equation:

$$\rho_{eff} C_{eff} \frac{\partial T}{\partial t} + \rho_f C_f \boldsymbol{v_f} \cdot \nabla T = \lambda_{eff} \nabla^2 T + H_M, \tag{2}$$

where C is the specific heat, and λ is the thermal conductivity. ρ_{eff}, C_{eff}, and λ_{eff} are effective properties of water-saturated rocks, obtained by averaging the properties of the hydrothermal fluids (weighted by the porosity ϕ) and the dry matrix (1-ϕ). H_M is the term for latent heat from magma crystallization.

Our numerical domain is 24 km high and 10 km wide (discretized as 100-m wide cells). It allows no conductive heat flow through its sides and is heated at its base to a constant temperature of 1,250°C. The top boundary represents the seafloor corresponding to a hydrostatic pressure $P_0 = 20$ MPa, which allows fluids to escape with no conductive flux and 0°C fluids to enter the lithosphere. The thermodynamic properties of the hydrothermal fluids correspond to those of a 3.2 wt.% NaCl–H_2O mixture (Anderko & Pitzer, 1993; Pitzer et al., 1984). The viscosity of the hydrothermal fluid is approximated as that of pure water, following the parameterization of Holzbecher (1998). The initial temperature field (at $t = 0$) is set to linearly increase from 0°C to 1,000°C (basaltic solidus T_S; Sinton & Detrick, 1992) between the seafloor and a depth of 10 km, and to linearly increase from 1,000°C to the imposed bottom temperature of 1,250°C between 10 km depth and the bottom of the domain (Figure 2a).

2.2. Permeable Hydrothermal System

Hydrothermal convection requires fluids pathways that account for sufficient permeability in lithospheric rocks. Thermal and tectonic stresses can induce fracturing on a range of scales, which can in turn lead to the establishment of a connected, permeable fracture network. High temperatures and pressure, however, are not conducive to cracking, because thermally activated creep (at temperatures exceeding a visco-elastic transition T_{ve}) relaxes the stresses that lead to fracturing, and because pressure opposes the opening of mode-I fractures (e.g., Demartin et al., 2004). Thus, the extent of the domain accessible to hydrothermal convection should be limited both in depth and temperature, with crucial implications for the resulting thermal regime. To describe this, we adopt a model in which rocks become permeable when their stress state enables the stable propagation of fractures from pre-existing, grain-scale flaws (Fredrich & Wong, 1986), that is, when the stress intensity factor around flaws reaches the fracture toughness of the material K_{IC}. This implicitly assumes that the formation of a permeable framework rapidly follows the growth of a pervasive network of micro-cracks. As our numerical model of convection does not handle deformation nor stresses within the rock matrix, we parameterize a thermal stress proportional to the amount of cooling below T_{ve}. Combining this driving stress with confining pressure (resisting stress), we express the stress intensity factor at any point in the domain as a function of temperature and depth (Demartin et al., 2004; Fredrich & Wong, 1986; Olive & Crone, 2018). The (shallow) domain where this stress intensity factor exceeds K_{IC} is assigned a uniform permeability k (Figure 2b), and hosts hydrothermal convection modeled as Darcy porous flow. The underlying domain is kept impermeable and transfers heat conductively.

This approach constitutes a middle ground between imposing temperature and imposing heat flow at the base of the convective domain. It also allows the base of the convective region (a percolation front located at depth Z_H) to evolve through time in a manner that depends on its temperature (T_H). We adopt the parameterization of Olive and Crone (2018) and Fan et al. (2021), which expresses the balance between cooling stresses and confining pressure as:

$$A_T(T_{ve} - T_H) - A_P(P_0 + \rho g Z_H) = K_{IC}, \tag{3}$$

where A_T and A_P are sensitivity coefficients of the cooling stress and confining pressure, respectively (both depend on micro-mechanical parameters such as grain size) and ρ is the lithosphere density. Rather than exploring the effect of micro-mechanical parameters on the values of A_T, A_P, and the resulting dynamics of the cracking front (e.g., Demartin et al., 2004; Olive & Crone, 2018), we use the same value of A_T as Fan et al. (2021) and empirically adjust A_P to define the maximum hydrothermal domain depth (Z_{H0}; dashed blue lines in Figure 2a), that is, the maximum depth of the cracking front (corresponding to $T_H = 0$°C in Equation 3). According to Equation 3, a lower A_P corresponds to a higher slope of the straight line between (T_{ve}, 0) and (0, Z_H) (solid blue lines in Figure 2a), suggesting that for the same accumulated cooling stress (i.e., the same T_H), fractures experience less resistance from confining pressure, and the cracking front can reach greater depths.

2.3. Magmatic Heat Input

In addition to fixing the temperature at the base of the domain, we supply magmatic heat to the domain in the form of repeated AML injection events. These consist of instantaneously resetting temperature to the liquidus T_M within a domain of vertical and horizontal extents H_{AML} and W_{AML}, respectively, every time interval τ (Fan et al., 2021). We choose T_M as 1,200°C, based on the average composition of the MORB (Sinton & Detrick, 1992). Lower or greater T_M could represent more or less evolved magma, resulting from higher or lower degrees of melting. The imposed AML is always centered in the horizontal direction, and its top coincides with the isotherm *Tr*. *Tr* is the melt emplacement temperature of the host rock, or more explicitly, the temperature of the isotherm at which melt is emplaced. *Tr* is a key parameter that we will systematically vary in this work. Our simulations keep tracks of melt fraction, assumed to be a linear function of temperature between the basaltic solidus T_S and the liquidus at T_M.

Following the approach of Fontaine et al. (2011) and Fan et al. (2021), a latent heat term, that is, the H_M term in Equation 2, is expressed in the energy equation when rocks cool between T_M and T_S:

$$H_M = \frac{-L\rho_M}{T_M - T_S}\frac{\partial T}{\partial t}\lceil x_L \rceil, \tag{4}$$

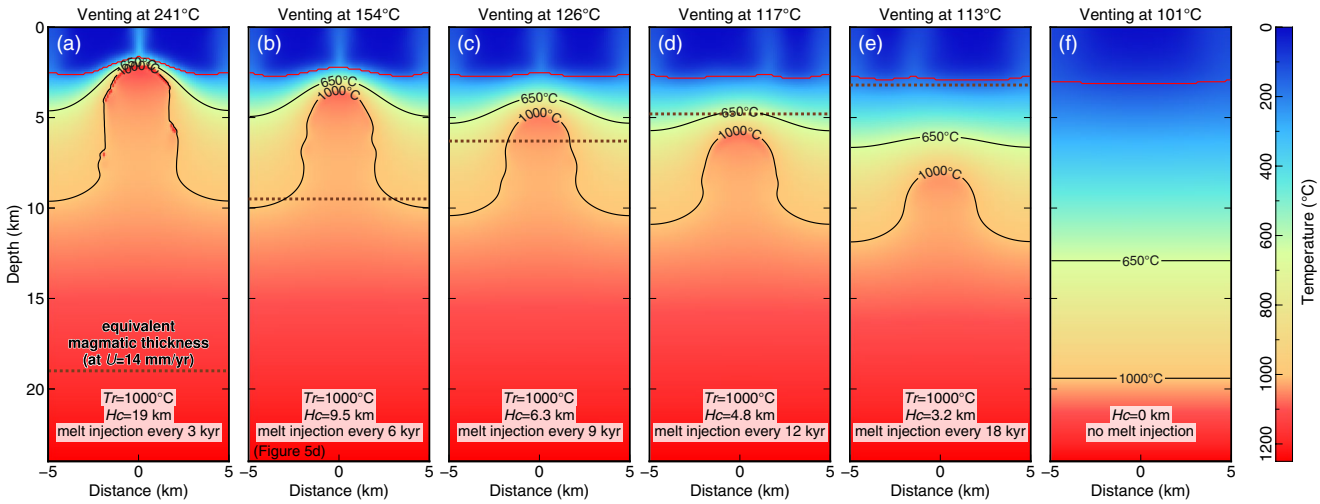

Figure 3. (a)–(e) Snapshots of stationary-state thermal regimes for simulations, varying time intervals of melt injection from τ = 3, 6, 9, 12, to 18 kyr, corresponding to Hc = 19, 9.5, 6.3, 4.8, and 3.2 km at the Southwest Indian Ridge (SWIR) spreading rate of 14 mm/yr (from Figures 3a–3e). The axial melt lens (AML) dimension is set to W_{AML} = 4 km and H_{AML} = 0.2 km, emplaced beneath Tr = 1,000°C. Hydrothermal domains are confined above Z_{H0} = 3 km with a permeability of $k = 10^{-15}$ m^2. Red lines indicate cracking fronts. Black lines indicate the 650 and 1,000°C isotherms. The equivalent magmatic thicknesses are between the seafloor and dashed brown lines. (f) Snapshot of the stationary-state thermal regime with the same configuration of the hydrothermal domain but no melt injection. Tr, temperature of host rock upon melt emplacement; Hc, equivalent magmatic thickness.

where L is the latent heat, ρ_M is the magma density, and x_L is the local melt fraction, which is updated every time step to match the evolving temperature field ($x_L = 0$ at $T = T_S$, and $x_L = 1$ at $T = T_M$). We use the $\lceil x_L \rceil$ term in Equation 4 to make sure that the latent heat is considered only where the melt is present ($0 < x_L \leq 1$, i.e., $\lceil x_L \rceil = 1$). The latent heat, in addition to the specific heat of magma and hot rocks, fuels hydrothermal convection above depth Z_H.

The dimensions and frequency of melt intrusions are not set arbitrarily, as they must be compatible with the inferred melt supply of slow and ultraslow spreading ridges. Melt flux at a ridge section can be expressed as:

$$U\,Hc = \frac{W_{AML} H_{AML}}{\tau}, \tag{5}$$

where U is the full spreading rate and Hc is the equivalent magmatic (crustal) thickness. Assuming W_{AML} = 4 km and H_{AML} = 0.2 km, the 9.5-km thick crust at the SWIR 50°28'E (Jian et al., 2017) corresponds to a time interval of τ = 6 kyr, and the ~7.5-km thick crust at the Lucky Strike segment of the MAR (Seher et al., 2010) corresponds to a time interval of τ = 5.1 kyr (U = 21 mm/yr; Figures 1d and 2c).

We chose the model height of 24 km by running initial simulations with a maximum hydrothermal domain depth of Z_{H0} = 6 km, a permeability of $k = 10^{-15}$ m^2, and varied model heights. We ran these simulations with no melt injection until stationary states were reached and selected the model heights that placed the 650°C isotherm at a depth of 15 km, corresponding to the inferred BDT at the nearly amagmatic SWIR 64°30'E section (Figure S1b in Supporting Information S1; Chen et al., 2020). We note that this depth can also be obtained with a different model setup (e.g., Fan et al., 2021), in which the domain height is 30 km with an adiabatic bottom, the AML dimensions are set to W_{AML} = 5 km and H_{AML} = 0.4 km, and magmatic emplacement occurs every τ = 75 kyr beneath the isotherm Tr = 1,000°C (Figure 4b in Fan et al., 2021 and reproduced by this study in Figure S1a in Supporting Information S1).

We conducted four groups of simulations to explore different parameters associated with melt supply and hydrothermal circulation. These parameters correspond to numerical labels in Figures 2a and 2b. We take the magmatically robust SWIR 50°28'E, with its 9.5-km thick magmatic crust as a reference case. All simulations are run until reaching stationary states. The key parameters we vary are:

1. The frequency of melt injection ($1/\tau$; Figure 3 and Movie S1 in Supporting Information S1)

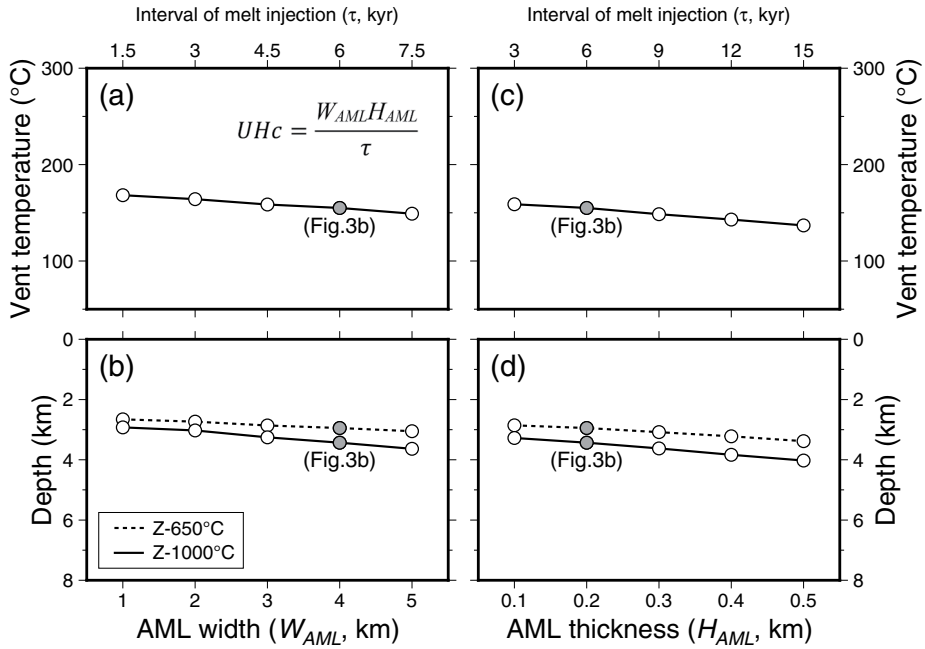

Figure 4. Effect of AML dimensions on key model outputs. (a) and (b) Simulations of changing W_{AML} from 1 to 5 km with a constant $H_{AML} = 0.2$ km. (c) and (d) Simulations of changing H_{AML} from 0.1 to 0.5 km with a constant $W_{AML} = 4$ km. In all simulations, τ is adjusted to keep a constant $Hc = 9.5$ km for the SWIR spreading rate of 14 mm/yr, according to Equation 5. AMLs are emplaced beneath $Tr = 1{,}000$°C, and hydrothermal domains are confined above $Z_{H0} = 3$ km with a permeability of $k = 10^{-15}$ m^2. (a) and (c) Maximum vent temperatures in stationary states. (b) and (d) Depths to the isotherms of 650°C (dashed lines) and 1,000°C (solid lines). See Figure S3 in Supporting Information S1 for the same configurations of AML dimensions but with a constant $Hc = 6.3$ km (for the SWIR spreading rate of 14 mm/yr).

2. AML dimensions with constant Hc (W_{AML} and H_{AML}; Figures 4 and S3 in Supporting Information S1 and Movies S2–S5 in Supporting Information S3)
3. The temperature of the host rock upon melt emplacement (Tr; Figures 5 and 6; Figure S4 in Supporting Information S1 and Movies S6–S14 in Supporting Information S3)
4. The maximum hydrothermal domain depth (Z_{H0}) and its permeability (k; Figures 7 and S5 in Supporting Information S1 and Movies S15–S18 in Supporting Information S3)

We also simulate cyclic variations in melt supply by alternately changing the frequency of melt injections (higher frequency during waxing magmatic phases and lower frequency during waning phases; Figures 8 and 9 and S6–S13 in Supporting Information S2 and Movies S19–S27 in Supporting Information S3). The model outputs of interest in all simulations include hydrothermal venting temperatures, the depths to the BDT (650°C isotherms) and to the mush zone (1,000°C isotherms), and the occurrence of mush zones at crustal depths.

3. Results

3.1. Frequency of Melt Injection

The first group of simulations explores the effect of varying the time interval between magmatic injections from $\tau = 3$, 6, 9, 12, to 18 kyr, corresponding to equivalent magmatic thicknesses of $Hc = 19$, 9.5, 6.3, 4.8, and 3.2 km at the SWIR spreading rate of 14 mm/yr, respectively (Figures 3a–3e). AML dimensions are set to $W_{AML} = 4$ km and $H_{AML} = 0.2$ km, and AMLs are emplaced beneath the $Tr = 1{,}000$°C isotherm, coinciding with the basaltic solidus. Another simulation with no melt injection is also run for reference (Figure 3f). Hydrothermal domains are confined above $Z_{H0} = 3$ km and have a permeability of $k = 10^{-15}$ m^2.

The melt-injection simulations are carried out for 3 Myr and the no-melt simulation for 20 Myr to ensure that all the thermal regimes reach stationary states independent from the initial condition. As the time interval increases from Figures 3a–3e (i.e., the frequency of melt injection and the equivalent magmatic thickness decrease), the

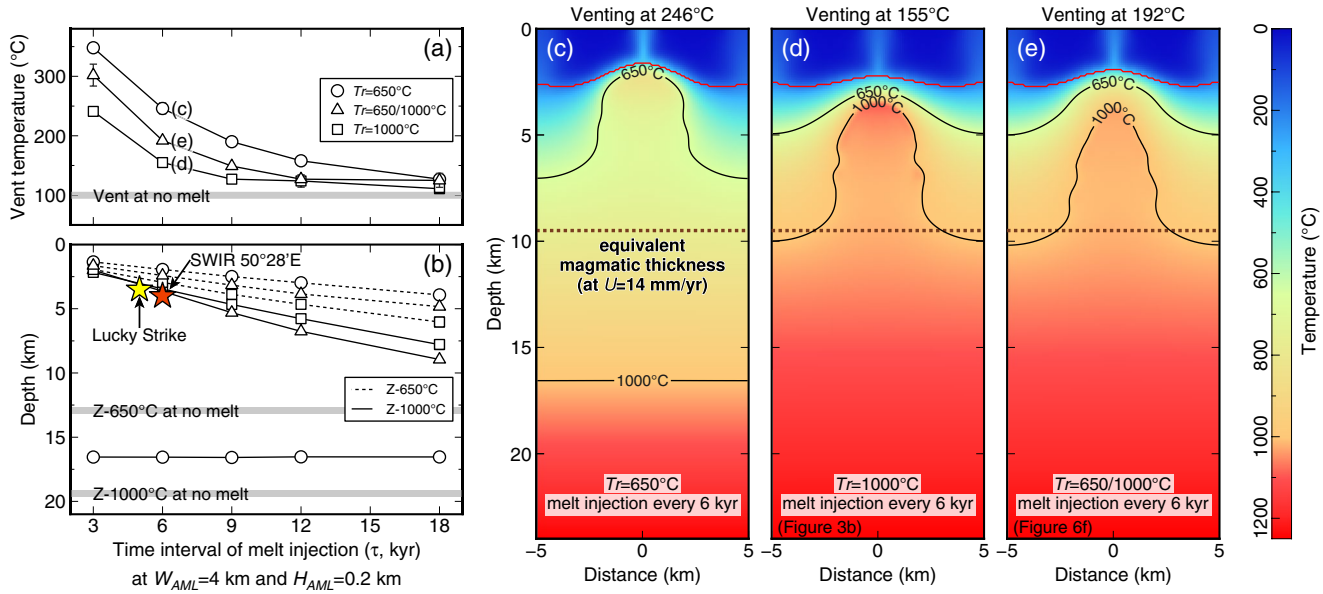

Figure 5. Simulations varying the temperature of the host rock upon melt emplacement: Tr = 650°C, Tr = 1,000°C, and Tr = 650/1,000°C (half of the melt emplaced at Tr = 650°C, and the other half at Tr = 1,000°C). See legend for symbols. Simulations with a given Tr have time intervals of melt injection varying from τ = 3, 6, 9, 12–18 kyr. The AML dimension is set to W_{AML} = 4 km and H_{AML} = 0.2 km in total. Hydrothermal domains are confined above Z_{H0} = 3 km with a permeability of $k = 10^{-15}$ m^2. (a) Maximum vent temperatures in stationary states. Thick gray line represents the no-melt simulation (Figure 3f). (b) Depths to the 650°C (dashed lines) and 1,000°C (solid lines) isotherms. Red and yellow stars represent the depths to the mush zones of the SWIR 50°28'E and the Lucky Strike. (c)–(e) Snapshots of stationary-state thermal regimes for three selected Tr at τ = 6 kyr. Equivalent magmatic thickness is shown for the SWIR spreading rate of 14 mm/yr. See Figure S4 in Supporting Information S1 for snapshots of τ = 3, 9, 12, and 18 kyr.

stationary-state thermal regimes become cooler and are characterized by a nonlinear decrease in hydrothermal vent (outflow) temperatures and a linear deepening of the 650 and 1,000°C isotherms (squares in Figures 5a and 5b, respectively). In simulations with τ = 3 and 6 kyr, extensive mush zones enclosed by the solidus (1,000°C) isotherms develop and persist at depths that match those of the lower crust for the corresponding equivalent crustal thicknesses of Hc = 19 and 9.5 km at the SWIR spreading rate (Figures 3a and 3b). By contrast, in simulations with τ = 12 and 18 kyr, the 1,000°C isotherms equilibrate at depths greater than the equivalent magmatic thickness of the crust at the SWIR spreading rate (Figures 3d and 3e).

3.2. AML Dimensions With Constant *Hc*

The second group of simulations examines the effect of varying W_{AML} from 1 to 5 km with a constant H_{AML} = 0.2 km (Figures 4a and 4b), as well as varying H_{AML} from 0.1 to 0.5 km with a constant W_{AML} = 4 km (Figures 4d and 4e). We adjust τ to keep the overall magma supply constant across these simulations, corresponding to an equivalent Hc = 9.5 km as set by Equation 5 for the SWIR spreading rate of 14 mm/yr. The AMLs are emplaced beneath Tr = 1,000°C, and hydrothermal domains are confined above Z_{H0} = 3 km with a permeability of $k = 10^{-15}$ m^2. We ran simulations for 3 Myr to reach stationary states. Hydrothermal vent temperatures and depths to the 650 and 1,000°C isotherms are found to slightly decrease with both the widening of W_{AML} at constant H_{AML}, and the thickening of H_{AML} at constant W_{AML} (Figure 4). Repeating these runs with a different reference magma supply (corresponding to Hc = 6.3 km at the SWIR spreading rate) and the same range of W_{AML} and H_{AML} gives very similar results in an overall cooler thermal regime (Figure S3 in Supporting Information S1). We conclude that the exact shape of the AML in our model has little influence on the axial thermal regime associated with a given magma flux, and we fix W_{AML} = 4 km and H_{AML} = 0.2 km in the following simulations.

3.3. Temperature of the Host Rock Upon Melt Emplacement

The third group of simulations (Figures 5 and S4 in Supporting Information S1) explores the effect of three selected temperatures of host rock upon melt emplacement (Tr): Tr = 650°C (a single AML emplaced beneath the 650°C isotherm during each injection event), Tr = 1,000°C (a single AML emplaced beneath the 1,000°C

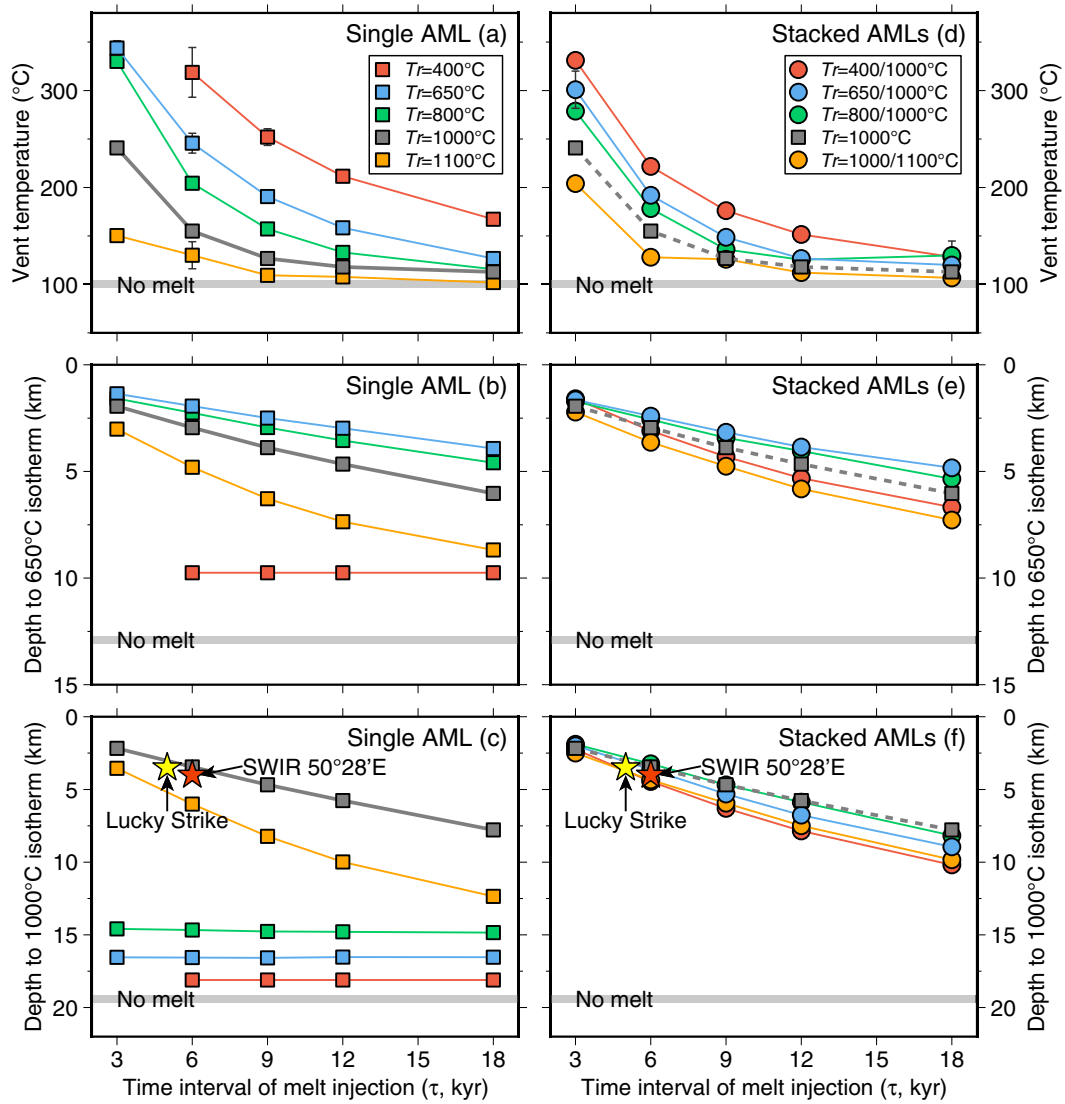

Figure 6. Key model outputs of simulations that vary the temperature of the host rock upon melt emplacement (*Tr*). See legend for the corresponding *Tr* values. Simulations with a given *Tr* have time intervals of melt injection varying from $\tau = 3$, 6, 9, 12, to 18 kyr. The axial melt lens (AML) dimension is set to $W_{AML} = 4$ km and $H_{AML} = 0.2$ km in total. Hydrothermal domains are confined above $Z_{H0} = 3$ km with a permeability of $k = 10^{-15}$ m^2. (a)–(c) Single AML emplacement. (d)–(e) Two stacked half-thick AMLs emplacements.

isotherm), and *Tr* = 650/1,000°C (two stacked half-thick AMLs emplaced beneath the 650 and 1,000°C isotherms at the same time during each injection event). Simulations with a given *Tr* have injection periods varying from $\tau = 3$, 6, 9, and 12–18 kyr. The AMLs are set to $W_{AML} = 4$ km and $H_{AML} = 0.2$ km (which amounts to two 0.1-km thick AMLs in the *Tr* = 650/1,000°C simulations). Hydrothermal domains are confined above $Z_{H0} = 3$ km with a permeability of $k = 10^{-15}$ m^2. Simulations with *Tr* = 1,000°C were previously presented as part of the first group of simulations (Figures 3a–3e). A control set of simulations was run with no melt injection (Figures 3f, 5a and 5b).

As in the *Tr* = 1,000°C simulations, the *Tr* = 650°C and *Tr* = 650/1,000°C simulations show nonlinear decreases in vent temperatures with increasing τ values, and linear decreases in the depths to the 650°C isotherms (Figures 5a and 5b). The 1,000°C isotherms in the *Tr* = 650/1,000°C simulations also linearly deepen with increasing τ, while in the *Tr* = 650°C simulations, the depth to the 1,000°C isotherm is constant at 16.5 km with no sensitivity to τ (Figure 5b). The *Tr* = 650°C and *Tr* = 650/1,000°C simulations also develop a transient, shallow region at

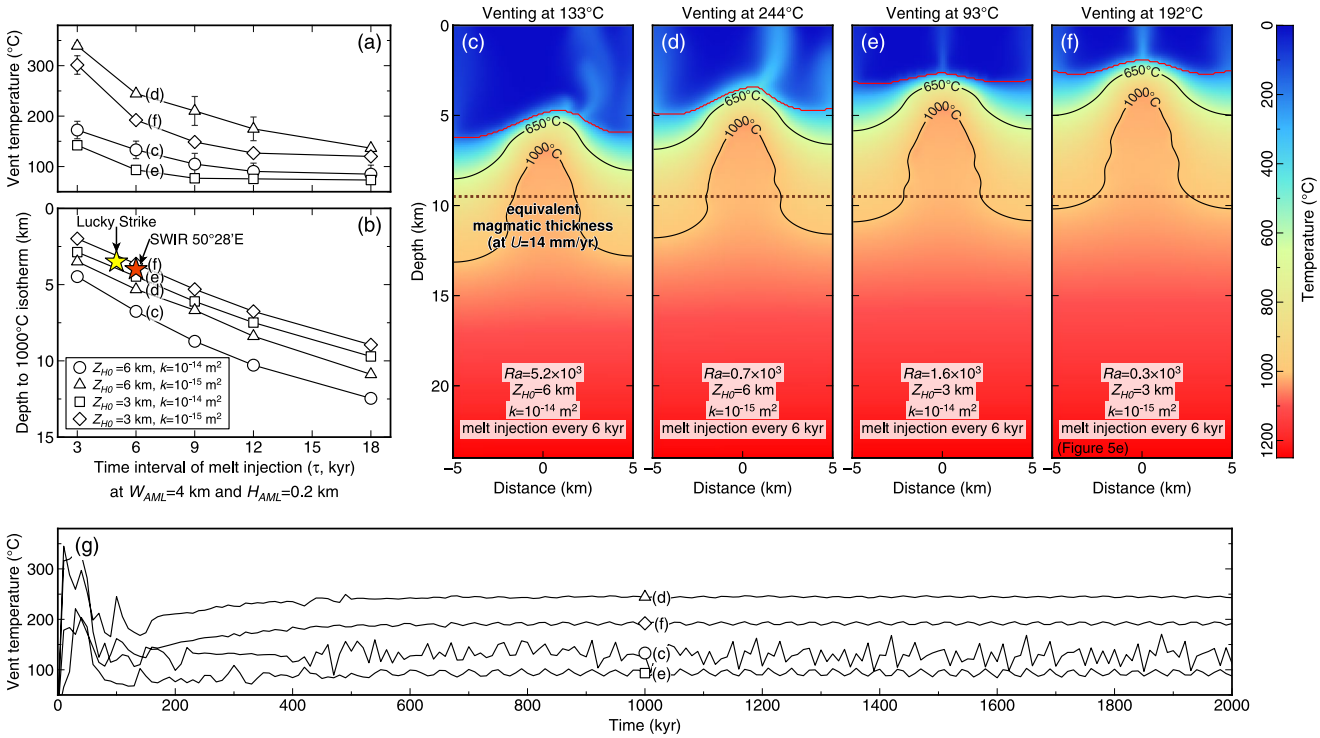

Figure 7. Simulations of four combinations of the maximum hydrothermal domain depths (Z_{H0} = 3 and 6 km) and permeabilities ($k = 10^{-15}$ and 10^{-14} m^2). See legend for symbols. Each combination has time intervals of melt injection varying from τ = 3, 6, 9, 12, to 18 kyr. The AML dimension is set to W_{AML} = 4 km and H_{AML} = 0.2 km in total, emplaced beneath Tr = 650/1,000°C. (a) Maximum vent temperatures in stationary states. (b) Depths to the 1,000°C isotherms. (c)–(f) Snapshots of stationary-state thermal regimes for four combinations at τ = 6 kyr. The equivalent magmatic thickness is calculated for the SWIR spreading rate of 14 mm/yr. (g) Maximum vent temperatures throughout the first 2,000 kyr of simulations for four combinations. *Ra*: Rayleigh number of hydrothermal convection system. See Figure S5 in Supporting Information S1 for snapshots of τ = 3, 9, 12, and 18 kyr.

temperatures in excess of 1,000°C, which appears just below the 650°C isotherms whenever melt is emplaced (Movie S6 in Supporting Information S3).

Keeping τ constant at 6 kyr (Hc = 9.5 km at the SWIR spreading rate), the Tr = 650°C simulations produce the shallowest 650°C isotherms but the deepest 1,000°C isotherms (Figures 5c–5e; see Figure S4 in Supporting Information S1 for other τ). The conductive boundary layer separating the cracking front from the 650°C isotherm is thinnest in the Tr = 650°C simulations, efficiently transporting heat from the AML to the hydrothermal system and hence producing the hottest vent temperatures (Figure 5a). In other words, the Tr = 650°C simulations produce the hottest upper lithospheres and the coldest lower lithospheres, alongside the highest hydrothermal vent temperatures and transient shallow mush zones (Figure 5c). In contrast, the Tr = 1,000°C simulations produce the coldest upper lithospheres, the lowest vent temperatures, and persistent crystal mush zones (regions in excess of 1,000°C) at depths shallower than the corresponding equivalent crustal thickness (Figure 5d).

The thermal regimes of the Tr = 650/1,000°C simulations have characters of the other two (Figure 5e). Like the Tr = 650°C simulations, the shallow half-AML produces a transient mush zone and moderate vent temperatures. Like the Tr = 1,000°C simulations, the deep half-AML enables a persistent mush zone at crustal depths (Figures 5a and 5b).

A wider range of Tr is explored with emplacements of a single AML and of two stacked half-thick AMLs (Figure 6). Both modes of AML emplacements show increased vent temperatures with the decrease of Tr (i.e., increasing Hc at a given spreading rate; Figures 6a and 6d). Simulations of Tr > 800°C cannot produce black-smoker (i.e., >300°C) hydrothermal vents at any given τ (Figure 6a). In the simulations with a single AML emplacement at $Tr \geq$ 650°C, melt emplaced closer to the 650 and 1,000°C isotherms leads to shallower 650 and 1,000°C isotherms, respectively (Figures 6b and 6c). The simulations with Tr < 1,000°C produce deep 1,000°C isotherms with no sensitivity to τ, and the larger the deviation from Tr = 1,000°C, the deeper the 1,000°C

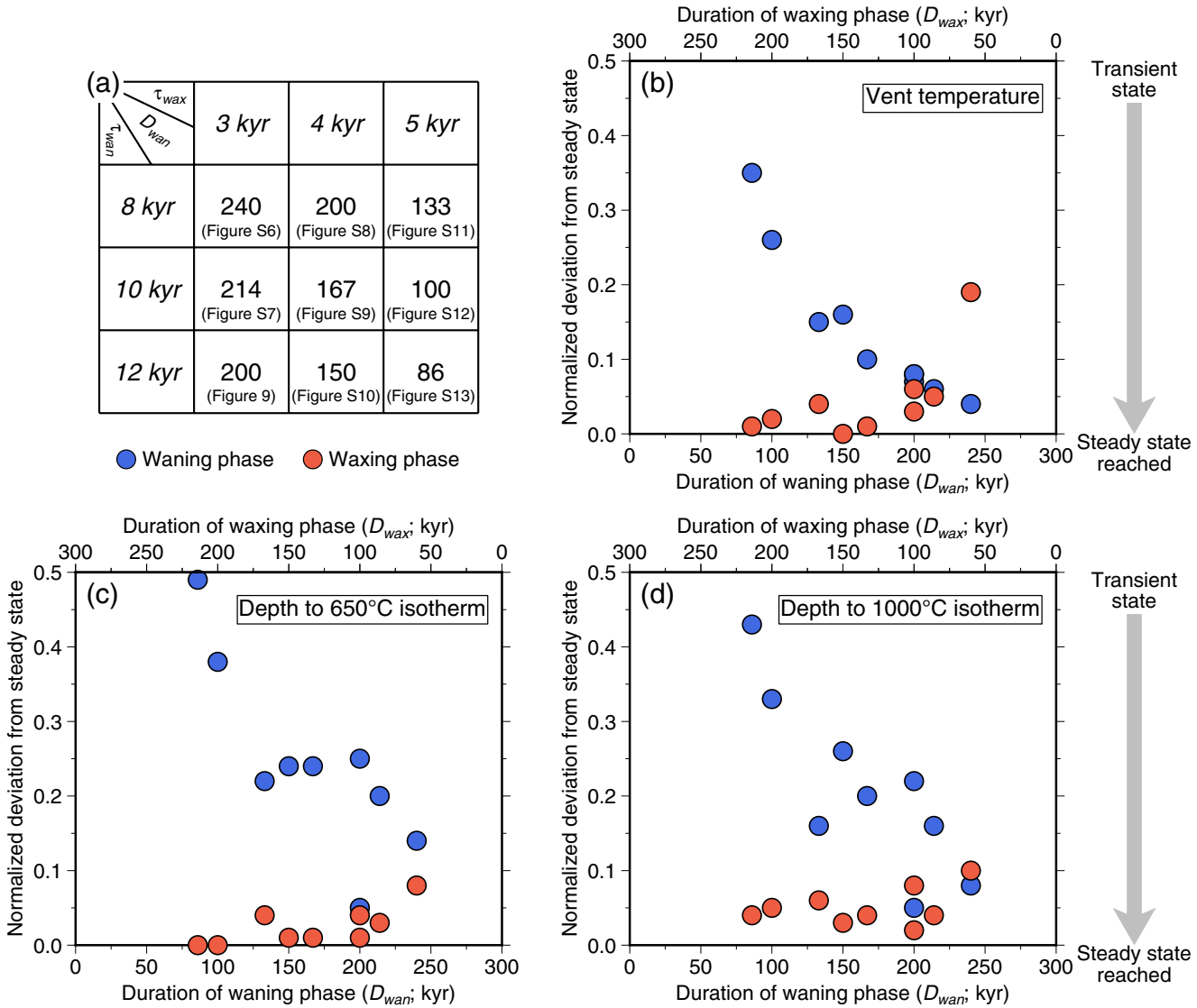

Figure 8. (a) 3×3 matrix of configurations of τ_{wax} = 3, 4, and 5 kyr and τ_{wan} = 8, 10, and 12 kyr. D_{wan} and D_{wax} are calculated by combining Equations 6 and 7. (b)–(d) Normalized deviations of vent temperature, and depths to the 650°C and 1,000°C isotherms, calculated by differences between values at the end of waxing (or waning) phases and at the steady state of the control simulation with $\tau = \tau_{wax}$ (or $\tau = \tau_{wan}$), which are normalized by the difference between two control simulations. τ_{wax}: time interval of melt injections during waxing phases. τ_{wan}: time interval of melt injections during waning phases. D_{wax}: duration of a waxing phase. D_{wan}: duration of a waning phase.

isotherms (Figure 6c). The simulations with Tr > 1,000°C produce overall colder thermal regimes than the Tr = 1,000°C simulations, because less heat is released by magma cooling and crystallization. The Tr = 400°C simulations produce the deepest 650°C isotherms, with no sensitivity to τ (no measurements at τ = 3 kyr because the 400°C isotherm in the model reaches the seafloor at such high equivalent melt supply). In the simulations of stacked AML emplacements, the changes of Tr have less impact on the depths to the 650 and 1,000°C isotherms, relative to the single AML emplacement, and this impact decreases as τ decreases until the differences are nearly zero at τ = 3 kyr (Figures 6e and 6f).

3.4. Hydrothermal System Extent and Permeability

The fourth group of simulations explores four combinations of two maximum hydrothermal domain depths Z_{H0} (3 and 6 km) and two permeabilities k (10^{-15} and 10^{-14} m^2; Figure 7). AML sizes are set to W_{AML} = 4 km and H_{AML} = 0.2 km in total, and AMLs are emplaced in a stacked mode beneath Tr = 650/1,000°C. Each combination

has injection periods varying from $\tau = 3$, 6, 9, 12, to 18 kyr (corresponding to $Hc = 19$, 9.5, 6.3, 4.8, and 3.2 km, respectively, for the SWIR spreading rate).

Each combination shows a nonlinear decrease in vent temperature and a linear increase in depths to the 650 and 1,000°C isotherms as τ increases (Figures 7a and 7b). For a given value of τ (i.e., for the same magma supply at a constant spreading rate), for example, $\tau = 6$ kyr (Figures 7c–7f; see Figure S5 in Supporting Information S1 for other injection periods), increasing the permeability or the maximum depth of the hydrothermal domain essentially shifts the thermal regime downward (Figures 7a and 7b). However, increasing the hydrothermal domain maximum depth while reducing its permeability leads to higher venting temperatures (Figure 7a). Allowing a greater maximum depth for the hydrothermal circulation region also leads to a more dynamic convective system with more upwelling plumes (Figures 7c and 7d). A higher permeability leads to more unstable hydrothermal vent temperatures (Figure 7g), and this stability is also controlled by the maximum depth of the hydrothermal domain and the time intervals of melt injection (Figures S5g-1–S5g-4 in Supporting Information S1).

4. Cyclic Changes in Frequencies of Melt Injection

Here, we simulate cyclic changes in magma supply with alternating waxing and waning phases over a cycle of 300 kyr (D_{cycle}), which have been inferred from geological observations at the SWIR 50°28'E (Chen et al., 2021). We first define the time-average time interval of melt injection as $\bar{\tau}$= 6 kyr according to Equation 5, by setting $Hc = 9.5$ km, $W_{AML} = 4$ km, $H_{AML} = 0.2$ km, and $U = 14$ mm/yr. A cycle of magma supply fluctuation comprises a waxing phase (duration D_{wax}) and a waning phase (duration D_{wan}), amounting to a total duration (or period):

$$D_{cycle} = D_{wax} + D_{wan}. \tag{6}$$

To account for a given time-average magma supply over the entire cycle (corresponding to a cycle-averaged magmatic thickness $Hc = 9.5$ km), the injection periodicities during the waxing and waning phase (τ_{wax} and τ_{wan}) must satisfy the following relationship (e.g., Ito & Behn, 2008):

$$\frac{D_{cycle}}{\bar{\tau}} = \frac{D_{wax}}{\tau_{wax}} + \frac{D_{wan}}{\tau_{wan}}. \tag{7}$$

We ran simulations for a total of 3 Myr. During the first 1.5 Myr, we set $\tau = \bar{\tau}$ to make sure the thermal regime reaches the stationary state associated with the long-term averaged magma supply. During the next 1.5 Myr, we alternately change τ to $\tau = \tau_{wax}$ for a duration D_{wax} and then to $\tau = \tau_{wan}$ for a duration D_{wan}. We examine 9 combinations of the above parameters by setting τ_{wax} = 3, 4, and 5 kyr and τ_{wan} = 8, 10, and 12 kyr (Figure 8a). We also ran two control simulations for each configuration with $\tau = \tau_{wax}$ and $\tau = \tau_{wan}$, corresponding to the high and low endmembers in magma supply of oscillating cases and to equivalent magmatic thicknesses Hc_{wax} and Hc_{wan}, respectively. In all simulations, two stacked half-thick AMLs are simultaneously emplaced beneath the 650 and 1,000°C isotherms (i.e., Tr = 650/1,000°C). The hydrothermal domain is confined above $Z_{H0} = 3$ km and is assigned a permeability of $k = 10^{-15}$ m^2.

Figure 9 shows the results of the configuration with the greatest contrast between endmember magma supplies, that is, $\tau_{wax} = 3$ kyr and $\tau_{wan} = 12$ kyr, yielding $D_{wax} = 100$ kyr and $D_{wan} = 200$ kyr upon combining Equations 6 and 7. We expect that the variability of the thermal regime within a complete cycle should be limited by the steady states of the two control simulations with $\tau = 3$ kyr and $\tau = 12$ kyr, which were run previously as part of the simulations that vary the isotherm of melt emplacement Tr (triangles in Figures 5a and 5b). Their steady-state vent temperatures (301 ± 18°C and 127°C) and depths to the 650°C (1.6 and 3.8 ± 0.1 km) and 1,000°C (2.0 and 6.7 ± 0.1 km) isotherms are shown in Figures 9a and 9c, marked as "+" for $\tau = 3$ kyr and "–" for $\tau = 12$ kyr, respectively. Four complete cycles with time series of vent temperatures and depths to the 650°C and 1,000°C isotherms, clearly bracketed by the results of two control simulations, are also shown in Figures 9a and 9c.

During waxing phases, isotherms move upward rapidly at a near-constant velocity, resulting in shallowing of the AML, shrinking of the conductive boundary layer, and warming of the hydrothermal system (from Figures 9e–9g). For over 70% of the waxing phase, the thermal regime resembles the hot-endmember $\tau = 3$ kyr control simulation with the 1,000°C isotherm lying shallower than 4 km, and vent temperatures in excess of 200°C (Figures 9b and 9d). At the end of the waxing phase, the thermal regime almost reaches the steady state at the level of the constant $\tau = 3$ kyr control simulation. In contrast, during the waning phases, isotherms migrate

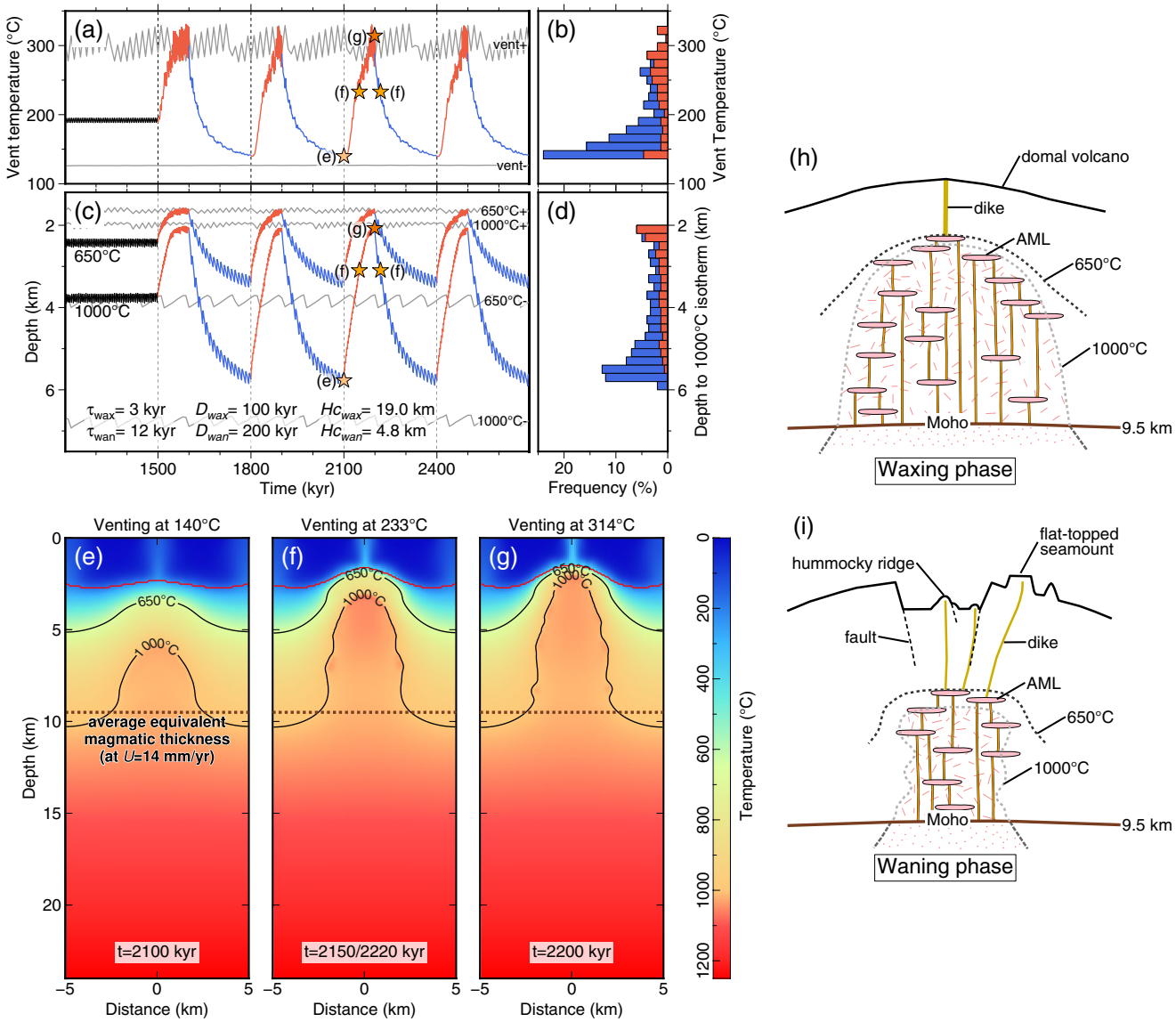

Figure 9. Simulation of cyclic changes in time intervals of melt injection. Time interval is set as $\bar{\tau}$ = 6 kyr for the first 1.5 Myr, and then set to alternating τ_{wax} = 3 kyr for D_{wax} = 100 kyr (Hc_{wax} = 19.0 km) and τ_{wan} = 12 kyr for D_{wan} = 200 kyr (Hc_{wan} = 4.8 km). See Figures S6-S13 for the other 8 configurations. The AML dimension is set to W_{AML} = 4 km and H_{AML} = 0.2 km in total, emplaced beneath Tr = 650/1,000°C. The hydrothermal domain is confined above Z_{H0} = 3 km with a permeability of $k = 10^{-15}$ m^2. (a) Maximum vent temperatures between 1,200 and 2,700 kyr. Red and blue lines represent waxing and waning phases, respectively. Gray lines represent two control simulations with τ_{wax} = 3 kyr (marked as vent+) and τ_{wan} = 12 kyr (marked as vent−). (b) Frequency of the maximum vent temperatures within a complete cycle. Red and blue bins represent waxing and waning phases, respectively. (c) Depth to the isotherms of 650°C and 1,000°C, distinct by labels. Gray lines represent the two control simulations for the depths to the isotherms of 650°C (marked as 650°C+ and 650°C−) and 1,000°C (marked as 1,000°C+ and 1,000°C−). (d) Frequency of the depth of 1,000°C isotherm within a complete cycle. (e)–(g) Snapshots (timing indicated in Figures 9a and 9c) of the thermal regimes at the end of a waning phase (2,100 kyr), middle of a waxing/waning phase (2,150/2,220 kyr), and end of a waxing phase (2,200 kyr). The time-average equivalent magmatic thickness is calculated for the SWIR spreading rate of 14 mm/yr. (h) and (i) Geological interpretations for waxing and waning phases at the SWIR 50°28'E, modified from Chen et al. (2021).

downward first rapidly, then more and more slowly over time (from Figures 9g–9e). In the simulations shown in Figure 9, the thermal regime does not have enough time to reach the steady state at the level of the τ = 12 kyr control simulation (Figures 9a and 9c). The thermal regime spends over 80% of the waning phase in states with the 1,000°C isotherm lying deeper than 4 km and vent temperatures <200°C (Figures 9b and 9d).

Figures 8b–8d quantify the extent to which the oscillatory thermal regimes described above deviate from their respective endmember steady states depending on the respective durations of the waxing and waning phase of the magmatic cycle (Figure 8a). Specifically, for each observable of interest (depths to the 650 and 1,000°C

isotherms, and vent temperatures), we measure the deviation between the values at the ends of waxing or waning phases and at the steady states of the control simulations with $\tau = \tau_{wax}$ or $\tau = \tau_{wan}$, respectively. All results are normalized by the difference between the two steady-state values. We find that the normalized deviations of all observables during waning phases decrease significantly as D_{wan} increases (Figures 8b–8d). This is simply because the longer duration of D_{wan} leaves more time for the system to approach the steady state. The shortest value of D_{wan} = 86 kyr (i.e., τ_{wax} = 5 kyr and τ_{wan} = 12 kyr; Figure 8a) leads to the largest normalized deviations from the cold-endmember steady state. Only two configurations have waning phases almost reaching (all deviations <0.1) the cold-endmember steady state, that is, τ_{wax} = 4 kyr and τ_{wan} = 8 kyr (D_{wan} = 200 kyr) and τ_{wax} = 3 kyr and τ_{wan} = 8 kyr (D_{wan} = 240 kyr). By contrast, the corresponding waxing phases are in most runs long enough to allow the thermal regime to reach or nearly reach (all deviations <0.1) the hot-endmember steady state (Figures 8b–8d).

5. Discussion

Our numerical modeling illustrates that not only the frequencies but also the depths of magmatic intrusions make a significant difference for the axial thermal regime at slow and ultraslow spreading ridges. Modes of melt injection (i.e., preferentially into cold or hot host rocks) provide an additional potential control for the variability of the axial thermal regime and a guideline for the formation of black-smoker hydrothermal circulation. The modeling of a cyclic melt supply shows that the thermal regime is significantly altered between waxing and waning phases, in a manner consistent with geological observations at the SWIR 50°28'E (Chen et al., 2021). This cyclic simulation also opens new perspectives on how the lower crust may be accreted at slow and ultraslow spreading ridges. Finally, we discuss the advantages and shortcomings of our treatment of hydrothermal convection.

5.1. Melt Emplacement Controls on the Axial Thermal Regime

The thermal regime of MORs has been predicted to be overall hotter with the increasing spreading rate, that is, increasing melt supply assuming a constant magmatic crustal thickness (Phipps Morgan & Chen, 1993; Theissen-Krah et al., 2011). Our simulations reproduce these previous numerical predictions (Figure 3) and are consistent, for example, with variations in BDT depths along the Knipovich Ridge, where the maximum depth of earthquakes is overall shallower at magmatic than at amagmatic ridge sections (Meier et al., 2021). We also successfully predict the persistence of a lower-crustal mush zone (enclosed by the 1,000°C isotherm) at the center of the magmatically robust SWIR 50°28'E and Lucky Strike segments, a persistence that was not predicted for slow and ultraslow rates by previous thermal models (Phipps Morgan & Chen, 1993; Theissen-Krah et al., 2011).

However, changes in melt supply alone cannot explain why the maximum depth of earthquakes at the more magmatic Dragon Horn detachment of the SWIR is similar to or greater than at the nearly amagmatic endmember 64°30'E region of the same ridge (18 vs. 15 km; Chen et al., 2020; Tao et al., 2020; Yu et al., 2018), while spreading rates are the same. Here, we show that the depth of melt emplacement, which we represent by the melt emplacement temperature (*Tr*, or temperature of the host rock upon melt emplacement), adds a new degree of freedom to the modeled thermal regimes (Figure 6). When melt is emplaced at a low *Tr* (e.g., 650°C or less), the heat brought by the melt almost only warms the lithosphere above the *Tr* isotherm and is efficiently removed by hydrothermal circulation, while the lithosphere below is not heated. This effect, which had been conceptually proposed based on geological data (Cannat et al., 2019), provides a potential explanation for why the 18-km thick seismogenic lithosphere at the Dragon Horn segment of the SWIR (Tao et al., 2020; Yu et al., 2018) is similar in thickness to the seismogenic lithosphere in the nearly amagmatic 64°30'E ridge region (≥15 km; Chen et al., 2020): melt there may be mostly emplaced at shallow depths in cool host rocks, fueling robust hydrothermal circulation evidenced by numerous black smokers (Copley et al., 2016; Tao et al., 2012). This interpretation was proposed by Fan et al. (2021). It differs from that of Tao et al. (2020), calling for a permeable detachment fault that mines heat from a magma source lying at the BDT. We note, however, that our coldest run (no melt, and a maximum depth of Z_{H0} = 6 km and a permeability of $k = 10^{-14}$ m^2 for the hydrothermal system) predicts a BDT at 15.5 km, similar to the run with an equivalent magmatic crust of ~3 km (Zhao et al., 2013), melt emplaced at *Tr* = 400°C, and the SWIR spreading rate (a plausible context for the Dragon Horn; Figure S2 in Supporting Information S1). Such a configuration, therefore, leads to a thick axial lithosphere even with a non-zero melt supply.

5.2. Perspective on Lower-Crustal Construction Through Cyclic Melt Supply

Cyclic changes of melt supply with alternating waxing and waning phases over periods on the order of a few 100 kyr have been documented at some magmatically robust, segment-centered volcanos, such as ∼300 kyr at the SWIR 50°28'E (Chen et al., 2021) and 300–500 kyr at the Menez Gwen areas of the MAR (Klischies et al., 2019). Our simulations of cyclic changes of melt injection frequencies for the reference case of the SWIR 50°28'E show an oscillatory thermal regime with a ∼4 km fluctuation of the depth to the 1,000°C isotherm during waxing and waning phases (Figures 9c and 9d). In this simulation, the waxing phases last 100 kyrs, and the waning phases last 200 kyrs, which correspond to the accretion of only 1.4 and 2.8 km of new lithospheres at the SWIR spreading rate.

During waning phases, each newly injected AML is emplaced beneath its predecessor as the ridge axis cools, the hydrothermal domain deepens, and the mush zone gradually subsides to greater depths. During waxing phases, each newly injected AML is emplaced above its partly crystallized predecessor and into material that crystallized toward the end of the previous waning phase, including hydrothermally altered materials and dikes that fed the hummocky ridges typical of waning phases (Chen et al., 2021), and the top of the mush zone ascends until the thermal regime reaches a stationary state. Over the whole cycle, the lower crust is therefore constructed by a sequence of melt lenses emplaced at progressively shallower depths during the waxing phase and then at progressively deeper depths during the waning phase, while the upper lithosphere cools and crystallizes, and a progressively deeper BDT results in faulting of the crystallized material. We would expect differences in this crustal construction scheme depending on the duration of waxing and waning phases, resulting in different amplitudes for the oscillatory thermal regime and on the spreading rates, resulting in changes in the width of the affected new lithosphere.

Overall, this mode of lower-crustal construction would result in complex melt-rock interactions and in the assimilation of previously cooled, variably tectonized, and hydrothermally altered gabbros and dikes. The periodicity of melt supply and the fluctuation of the thermal regime documented at fast spreading ridges (Marjanović et al., 2014; Soule et al., 2009) are much lower than at slow and ultraslow ridges (Chen et al., 2021; Klischies et al., 2019). The predictions of our simulations are, however, consistent with the dynamics of magmatic systems documented at the gabbro/sheeted dikes transition zones of the Oman ophiolite and the fast spreading East Pacific Rise (Carbotte et al., 2021; Gillis, 2008; Nicolas et al., 2008). The AMLs migrate upward during waxing phases, corresponding to the reheating of the AML roof and hence the recrystallization of hydrothermally altered sheeted dikes into pyroxene and hornblende hornfels with the formation of xenoliths, while during waning phases, AMLs migrate downward, causing crystallization at the AML roof and/or sides to form isotropic gabbros that are crosscut by later dikes (France et al., 2009; Gillis, 2008; Nicolas et al., 2008, 2009). Samples of the lower crust formed at magmatically robust segment centers of slow and ultraslow ridges are lacking to compare to fast spread examples and test these predictions.

Time variations of the melt supply are also inferred at several less magmatically robust slow and ultraslow ridge sections, from systematic changes in seafloor morphology, volcanic facies, and apparent faulting patterns (Ballard & van Andel, 1977; Chen et al., 2021; Escartín et al., 2014; Klischies et al., 2019; MacLeod et al., 2009; Mendel et al., 2003; Parson et al., 1993). Axial Volcanic Ridges have been proposed to have a life cycle, constructed in magmatic periods and split in tectonic periods (Mendel et al., 2003; Parson et al., 1993), and melt-poor ridge sections with Oceanic Core Complexes (OCCs) also have cycles as the OCCs may be initiated by a local waning of melt supply and terminated by a higher melt supply (Cannat et al., 2009; MacLeod et al., 2009). The amplitude of these melt supply variations is, however, most probably lower than at the SWIR 50°28'E and Menez Gwen segment centers, with colder waxing phases and overall deeper mush zones and thicker brittle domains. Elements of the cyclic lower-crustal construction scheme we propose may still be relevant, but tectonic processes would thus play a much greater role. Overall, the lower-crustal construction and the thermal regime along slow and ultraslow spreading ridges can be expected to be conditioned by melt supply variations in both space and time, resulting in extreme variability.

5.3. Hydrothermal Convection

High-temperature (>300°C) black smokers at slow and ultraslow spreading ridges have been continuously documented over the last three decades (Beaulieu et al., 2015), including the highest vent temperatures (>400°C)

discovered at the MAR 5°S (Koschinsky et al., 2008) and at the Beebe vent field of the Mid-Cayman Spreading Center (Connelly et al., 2012). Vigorous black-smoker hydrothermal circulation is believed to extract heat from a hot magma body beneath, separated by a thin conductive boundary layer (e.g., Lowell et al., 2013; Wilcock et al., 2009). In our modeling, we do not predict high-temperature venting when melt is mostly emplaced at Tr = 1,000°C, because the hydrothermal heat extraction is impeded by a thick boundary layer. However, when we allow melt to be emplaced at a low Tr or ascribe a deeper Z_{H0} to the hydrothermal domain, the boundary layer is thinner, and black-smoker hydrothermal circulation may be active for several thousand years. This condition may be met at detachment fault systems with shallow intermittent gabbroic intrusions (Cannat et al., 2009; Ildefonse et al., 2007) and deep-reaching hydrothermal fluids (Andersen et al., 2015; Tao et al., 2020). It should be noted that changing permeability and accounting for heterogeneities in the permeability field could also directly change hydrothermal venting temperatures and the efficiency of hydrothermal heat removal in our simulations. We chose not to explore these parameters and to rely on our straightforward porous convection model, as was first attempted by Theissen-Krah et al. (2011) and later by Fan et al. (2021), Hasenclever et al. (2014), and Olive and Crone (2018).

In this approach, the properties of the hydrothermal fluids, the confining depth of the hydrothermal system (Demartin et al., 2004), and the critical fluid temperature at ~400°C (Jupp & Schultz, 2000) define the Rayleigh number (Ra), written as (Fontaine & Wilcock, 2007; Lowell & Germanovich, 2004):

$$Ra = \frac{\alpha_f g\ (T_H - T_0)\ Z_H k}{\kappa_m \nu_f}, \tag{8}$$

where α_f and ν_f are the thermal expansion coefficient and kinematic viscosity of the hydrothermal fluid, respectively, and κ_m is the effective thermal diffusivity of the fluid-rock system. Representative values of these parameters are listed in Table S1 in Supporting Information S1 and can be used to estimate the Rayleigh number.

In simulations varying the maximum depths and permeabilities of the hydrothermal system with the same melt supply (τ = 6 kyr), the combination of Z_{H0} = 6 km and $k = 10^{-14}$ m^2 produces the highest $Ra = 5.2 \times 10^3$, corresponding to the most unstable vent temperatures and multiple, chaotic hydrothermal plumes that move horizontally (Figures 7c and 7g). By contrast, at the lowest $Ra = 0.3 \times 10^3$, corresponding to the combination of Z_{H0} = 3 km and $k = 10^{-15}$ m^2, hydrothermal circulation is stable with a single, robust, and vertically upwelling plume (Figure 7f). The combination of Z_{H0} = 6 km and $k = 10^{-15}$ m^2 produces stable and elevated vent temperatures with horizontally moving plumes, corresponding to a relatively low $Ra = 0.7 \times 10^3$ (Figure 7d), and the combination of Z_{H0} = 3 km and $k = 10^{-14}$ m^2 produces a relatively high $Ra = 1.6 \times 10^3$, yet a single, weak, vertically upwelling plume (Figure 7e). Hydrothermal convection under different melt supplies (other τ) also produces different patterns of hydrothermal plumes and Rayleigh numbers (Figure S5 in Supporting Information S1). Consequently, we observe that hydrothermal plumes evolve differently in different simulations, presumably reflecting the realistic properties of hydrothermal convection. Therefore, although they do not explore the complex permeability structure of the natural systems, our simulations are a more accurate way of describing hydrothermal heat extraction compared to a Nusselt number approach (e.g., Phipps Morgan & Chen, 1993).

Finally, we note that our 2-D description of hydrothermal convection cannot capture inherently 3-D features of real hydrothermal systems, such as pipe-like flows, or recharge occurring both along- and across-axis (e.g., Coumou et al., 2008; Fontaine et al., 2014). Our parameterization, however, captures the first-order physics of heat transport by porous convection, as reviewed by Lowell and Germanovich (2004). These include the cellular structure of the flow, the non-linear dependence of heat extraction on basal temperature, and the juxtaposition of an adiabatic core and a conductive boundary layer. In this sense, our approach, which follows that of Theissen-Krah et al. (2011), provides a more realistic description of hydrothermal heat transfer compared to classical descriptions of convection as conduction enhanced by an ad-hoc Nusselt number (e.g., Phipps Morgan & Chen, 1993).

6. Conclusion

We used a 2D numerical thermal model (Fan et al., 2021) that couples repeated melt intrusions and hydrothermal convection to constrain the thermal regimes inferred from two magma supply endmembers at ultraslow spreading ridges: the most magmatically robust SWIR 50°28'E and the nearly amagmatic SWIR 64°30'E. The variability of

the thermal regimes at slow and ultraslow spreading ridges was explored by varying parameters associated with melt supply, modes of magma emplacement (i.e., the frequencies and depths of melt injections), and hydrothermal circulation (i.e., the maximum hydrothermal domain depth and permeability).

Unsurprisingly, our simulations predict that higher frequencies of melt injections result in overall hotter thermal regimes. The novelty in our results is that the depth of melt emplacement also plays a significant role; shallower melt injections result in greater efficiency of hydrothermal heat removal with black-smoker hydrothermal circulation and thus in a cooler thermal regime. This provides a potential explanation for the unexpected thick seismogenic lithosphere at the Dragon Horn area. Alternatively, deeper melt injections result in a hotter regime and are a condition for the formation of persistent lower-crustal mush zones. In addition, the increases of permeability and the maximum hydrothermal domain depth result in the increase of efficiency of hydrothermal heat removal, downward shifting the depths to the brittle-ductile transition and mush zone. We also explored the effect of cyclic changes in melt supply documented at the reference case of the SWIR 50°28'E on the persistence of the lower-crustal mush zone, the depth to the brittle-ductile transition, and the formation of the high-temperature hydrothermal vent, which provide insights into the lower-crustal construction at slow and ultraslow spreading ridges.

Data Availability Statement

All the MATLAB codes with input files to reproduce all the results are available on figshare (https://doi.org/10.6084/m9.figshare.16641973).

Acknowledgments
All models are run using MATLAB. Figures are generated using GMT 6 (Wessel et al., 2019). Jie Chen was supported by China Scholarship Council (201808330437). Support for this work was provided by ANR project Ridge Factory Slow (ANR-18-CE01-0002-01). This is IPGP contribution No. 4240.

References

Anderko, A., & Pitzer, K. S. (1993). Equation-of-state representation of phase equilibria and volumetric properties of the system NaCl-H2O above 573 K. *Geochimica et Cosmochimica Acta*, *57*, 1657–1680. https://doi.org/10.1016/0016-7037(93)90105-6

Andersen, C., Rüpke, L., Hasenclever, J., Grevemeyer, I., & Petersen, S. (2015). Fault geometry and permeability contrast control vent temperatures at the Logatchev 1 hydrothermal field, Mid-Atlantic Ridge. *Geology*, *43*, 51–54. https://doi.org/10.1130/G36113.1

Anderson, D. L. (1995). Lithosphere, asthenosphere, and perisphere. *Reviews of Geophysics*, *33*, 125. https://doi.org/10.1029/94RG02785

Ballard, R. D., & vanAndel, T. H. (1977). Morphology and tectonics of the inner rift valley at lat 36°50'N on the Mid-Atlantic Ridge. *Bulletin of the Geological Society of America*, *88*. https://doi.org/10.1130/0016-7606(1977)88<507:MATOTI>2.0.CO;2

Beaulieu, S. E., Baker, E. T., & German, C. R. (2015). Where are the undiscovered hydrothermal vents on oceanic spreading ridges? *Deep-Sea Research Part II: Topical Studies in Oceanography*, *121*, 202–212. https://doi.org/10.1016/j.dsr2.2015.05.001

Buck, W. R., Lavier, L. L., & Poliakov, A. N. B. (2005). Modes of faulting at mid-ocean ridges. *Nature*, *434*, 719–723. https://doi.org/10.1038/nature03358

Cannat, M., Mevel, C., Maia, M., Deplus, C., Durand, C., Gente, P., et al. (1995). Thin crust, ultramafic exposures, and rugged faulting patterns at the Mid-Atlantic Ridge (22°–24°N). *Geology*, *23*, 49. https://doi.org/10.1130/0091-7613(1995)023<0049:TCUEAR>2.3.CO;2

Cannat, M., Sauter, D., Escartín, J., Lavier, L., & Picazo, S. (2009). Oceanic corrugated surfaces and the strength of the axial lithosphere at slow spreading ridges. *Earth and Planetary Science Letters*, *288*, 174–183. https://doi.org/10.1016/j.epsl.2009.09.020

Cannat, M., Sauter, D., Lavier, L., Bickert, M., Momoh, E., & Leroy, S. (2019). On spreading modes and magma supply at slow and ultraslow mid-ocean ridges. *Earth and Planetary Science Letters*, *519*, 223–233. https://doi.org/10.1016/j.epsl.2019.05.012

Cannat, M., Sauter, D., Mendel, V., Ruellan, E., Okino, K., Escartin, J., et al. (2006). Modes of seafloor generation at a melt-poor ultraslow-spreading ridge. *Geology*, *34*, 605–608. https://doi.org/10.1130/G22486.1

Carbotte, S. M., Marjanović, M., Arnulf, A. F., Nedimović, M. R., Canales, J. P., & Arnoux, G. M. (2021). Stacked magma lenses beneath mid-ocean ridges: Insights from new seismic observations and synthesis with prior geophysical and geologic findings. *Journal of Geophysical Research: Solid Earth*, *126*, e2020JB021434. https://doi.org/10.1029/2020JB021434

Chen, J., Cannat, M., & Crawford, W. C. (2020). *Microseismicity constraints on brittle lithosphere thickness at a nearly amagmatic spreading corridor of the ultraslow Southwest Indian Ridge*. AGU Fall Meeting, Abstract No. T026-0013.

Chen, J., Cannat, M., Tao, C., Sauter, D., & Munschy, M. (2021). 780 thousand years of upper-crustal construction at a melt-rich segment of the ultraslow spreading Southwest Indian Ridge 50°28'E. *Journal of Geophysical Research: Solid Earth*, *126*. https://doi.org/10.1029/2021JB022152

Chen, Y. J. (1992). Oceanic crustal thickness versus spreading rate. *Geophysical Research Letters*, *19*, 753–756. https://doi.org/10.1029/92GL00161

Christeson, G. L., Goff, J. A., & Reece, R. S. (2019). Synthesis of oceanic crustal structure from two-dimensional seismic profiles. *Reviews of Geophysics*, *57*, 504–529. https://doi.org/10.1029/2019RG000641

Combier, V., Seher, T., Singh, S. C., Crawford, W. C., Cannat, M., Escartín, J., & Dusunur, D. (2015). Three-dimensional geometry of axial magma chamber roof and faults at Lucky Strike volcano on the Mid-Atlantic Ridge. *Journal of Geophysical Research: Solid Earth*, *120*, 5379–5400. https://doi.org/10.1002/2015JB012365

Connelly, D. P., Copley, J. T., Murton, B. J., Stansfield, K., Tyler, P. A., German, C. R., et al. (2012). Hydrothermal vent fields and chemosynthetic biota on the world's deepest seafloor spreading centre. *Nature Communications*, *3*. https://doi.org/10.1038/ncomms1636

Copley, J. T., Marsh, L., Glover, A. G., Hühnerbach, V., Nye, V. E., Reid, W. D. K., et al. (2016). Ecology and biogeography of megafauna and macrofauna at the first known deep-sea hydrothermal vents on the ultraslow-spreading Southwest Indian Ridge. *Scientific Reports*, *6*. https://doi.org/10.1038/srep39158

Corbalán, A., Nedimović, M. R., Louden, K. E., Cannat, M., Grevemeyer, I., Watremez, L., & Leroy, S. (2021). Seismic velocity structure along and across the ultraslow-spreading Southwest Indian ridge at 64°30'E showcases flipping detachment faults. *Journal of Geophysical Research: Solid Earth*, *126*, e2021JB022177. https://doi.org/10.1029/2021JB022177

Coumou, D., Driesner, T., & Heinrich, C. A. (2008). The structure and dynamics of mid-ocean ridge hydrothermal systems. *Science*, *80*, 321–1828. https://doi.org/10.1126/science.1159582

Demartin, B., Hirth, G., & Evans, B. (2004). Experimental constraints on thermal cracking of peridotite at oceanic spreading centers. In *Geophysical Monograph Series* (pp. 167–185). Blackwell Publishing Ltd. https://doi.org/10.1029/148GM07

Detrick, R. S., Buhl, P., Vera, E., Mutter, J., Orcutt, J., Madsen, J., & Brocher, T. (1987). Multi-channel seismic imaging of a crustal magma chamber along the East Pacific Rise. *Nature*, *326*, 35–41. https://doi.org/10.1038/326035a0

Dick, H. J. B. (1989). Abyssal peridotites, very slow spreading ridges and ocean ridge magmatism. *Geological Society, London, Special Publications*, *42*(1), 71–105. https://doi.org/10.1144/gsl.sp.1989.042.01.06

Dusunur, D., Escartín, J., Combier, V., Seher, T., Crawford, W., Cannat, M., et al. (2009). Seismological constraints on the thermal structure along the Lucky Strike segment (Mid-Atlantic Ridge) and interaction of tectonic and magmatic processes around the magma chamber. *Marine Geophysical Researches*, *30*, 105–120. https://doi.org/10.1007/s11001-009-9071-3

Escartín, J., Soule, S. A., Cannat, M., Fornari, D. J., Düşünür, D., & Garcia, R. (2014). Lucky Strike seamount: Implications for the emplacement and rifting of segment-centered volcanoes at slow spreading mid-ocean ridges. *Geochemistry, Geophysics, Geosystems*, *15*, 4157–4179. https://doi.org/10.1002/2014GC005477

Fan, Q., Olive, J. A., & Cannat, M. (2021). Thermo-mechanical state of ultraslow-spreading ridges with a transient magma supply. *Journal of Geophysical Research: Solid Earth*, *126*, e2020JB020557. https://doi.org/10.1029/2020JB020557

Fontaine, F. J., Cannat, M., Escartin, J., & Crawford, W. C. (2014). Along-axis hydrothermal flow at the axis of slow spreading Mid-Ocean Ridges: Insights from numerical models of the Lucky Strike vent field (MAR). *Geochemistry, Geophysics, Geosystems*, *15*, 2918–2931. https://doi.org/10.1002/2014GC005372

Fontaine, F. J., Olive, J. A., Cannat, M., Escartin, J., & Perol, T. (2011). Hydrothermally-induced melt lens cooling and segmentation along the axis of fast-and intermediate-spreading centers. *Geophysical Research Letters*, *38*. https://doi.org/10.1029/2011GL047798

Fontaine, F. J., & Wilcock, W. S. D. (2007). Two-dimensional numerical models of open-top hydrothermal convection at high Rayleigh and Nusselt numbers: Implications for mid-ocean ridge hydrothermal circulation. *Geochemistry, Geophysics, Geosystems*, *8*. https://doi.org/10.1029/2007GC001601

France, L., Ildefonse, B., & Koepke, J. (2009). Interactions between magma and hydrothermal system in Oman ophiolite and in IODP Hole 1256D: Fossilization of a dynamic melt lens at fast spreading ridges. *Geochemistry, Geophysics, Geosystems*, *10*. https://doi.org/10.1029/2009GC002652

Fredrich, J. T., & Wong, T. (1986). Micromechanics of thermally induced cracking in three crustal rocks. *Journal of Geophysical Research: Solid Earth*, *91*. https://doi.org/10.1029/jb091ib12p12743

Gillis, K. M. (2008). The roof of an axial magma chamber: A hornfelsic heat exchanger. *Geology*, *36*, 299–302. https://doi.org/10.1130/G24590A.1

Hasenclever, J., Theissen-Krah, S., Rüpke, L. H., Morgan, J. P., Iyer, K., Petersen, S., & Devey, C. W. (2014). Hybrid shallow on-axis and deep off-axis hydrothermal circulation at fast-spreading ridges. *Nature*, *508*, 508–512. https://doi.org/10.1038/nature13174

Holzbecher, E. O. (1998). Modeling density-driven flow in porous media, modeling density-driven flow in porous media. *Springer Science & Business Media*. https://doi.org/10.1007/978-3-642-58767-2

Ildefonse, B., Blackman, D. K., John, B. E., Ohara, Y., Miller, D. J., MacLeod, C. J., et al. (2007). Oceanic core complexes and crustal accretion at slow-speading ridges. *Geology*, *35*, 623. https://doi.org/10.1130/G23531A.1

Ito, G., & Behn, M. D. (2008). Magmatic and tectonic extension at mid-ocean ridges: 2. Origin of axial morphology. *Geochemistry, Geophysics, Geosystems*, *9*(9). https://doi.org/10.1029/2008GC001970

Jian, H., Chen, Y. J., Singh, S. C., Li, J., Zhao, M., Ruan, A., & Qiu, X. (2017). Seismic structure and magmatic construction of crust at the ultraslow-spreading Southwest Indian Ridge at 50°28'E. *Journal of Geophysical Research: Solid Earth*, *122*, 18–42. https://doi.org/10.1002/2016JB013377

Jupp, T., & Schultz, A. (2000). A thermodynamic explanation for black smoker temperatures. *Nature*, *403*, 880–883. https://doi.org/10.1038/35002552

Klischies, M., Petersen, S., & Devey, C. W. (2019). Geological mapping of the Menez Gwen segment at 37°50′N on the Mid-Atlantic Ridge: Implications for accretion mechanisms and associated hydrothermal activity at slow-spreading mid-ocean ridges. *Marine Geology*, *412*, 107–122. https://doi.org/10.1016/j.margeo.2019.03.012

Koschinsky, A., Garbe-Schönberg, D., Sander, S., Schmidt, K., Gennerich, H. H., & Strauss, H. (2008). Hydrothermal venting at pressure-temperature conditions above the critical point of seawater, 5°S on the Mid-Atlantic Ridge. *Geology*, *36*, 615. https://doi.org/10.1130/G24726A.1

Kuo, B. Y., & Forsyth, D. W. (1988). Gravity anomalies of the ridge-transform system in the South Atlantic between 31 and 34.5° S: Upwelling centers and variations in crustal thickness. *Marine Geophysical Researches*, *10*, 205–232. https://doi.org/10.1007/BF00310065

Langmuir, C., Humphris, S., Fornari, D., Van Dover, C., Von Damm, K., Tivey, M. K., et al. (1997). Hydrothermal vents near a mantle hot spot: The Lucky Strike vent field at 37°N on the Mid-Atlantic Ridge. *Earth and Planetary Science Letters*, *148*, 69–91. https://doi.org/10.1016/s0012-821x(97)00027-7

Li, J., Jian, H., Chen, Y. J., Singh, S. C., Ruan, A., Qiu, X., et al. (2015). Seismic observation of an extremely magmatic accretion at the ultraslow spreading Southwest Indian Ridge. *Geophysical Research Letters*, *42*(8), 2656–2663. https://doi.org/10.1002/2014gl062521

Lin, J., Purdy, G. M., Schouten, H., Sempere, J.-C., & Zervas, C. (1990). Evidence from gravity data for focused magmatic accretion along the Mid-Atlantic Ridge. *Nature*, *344*, 627–632. https://doi.org/10.1038/344627a0

Lowell, R. P., Farough, A., Hoover, J., & Cummings, K. (2013). Characteristics of magma-driven hydrothermal systems at oceanic spreading centers. *Geochemistry, Geophys. Geosystems*, *14*, 1756–1770. https://doi.org/10.1002/ggge.20109

Lowell, R. P., & Germanovich, L. N. (2004). Hydrothermal processes at mid-ocean ridges: Results from scale analysis and single-pass models. In *Geophysical Monograph Series* (pp. 219–244). Blackwell Publishing Ltd. https://doi.org/10.1029/148GM09

MacLeod, C. J., Searle, R. C., Murton, B. J., Casey, J. F., Mallows, C., Unsworth, S. C., et al. (2009). Life cycle of oceanic core complexes. *Earth and Planetary Science Letters*, *287*, 333–344. https://doi.org/10.1016/j.epsl.2009.08.016

Marjanović, M., Carbotte, S. M., Carton, H., Nedimović, M. R., Mutter, J. C., & Canales, J. P. (2014). A multi-sill magma plumbing system beneath the axis of the East Pacific Rise. *Nature Geoscience*, *7*, 825–829. https://doi.org/10.1038/ngeo2272

McKenzie, D., Jackson, J., & Priestley, K. (2005). Thermal structure of oceanic and continental lithosphere. *Earth and Planetary Science Letters*, *233*, 337–349. https://doi.org/10.1016/j.epsl.2005.02.005

Meier, M., Schlindwein, V., Scholz, J. R., Geils, J., Schmidt-Aursch, M. C., Krüger, F., et al. (2021). Segment-scale seismicity of the ultraslow spreading Knipovich Ridge. *Geochemistry, Geophysics, Geosystems*, *22*. https://doi.org/10.1029/2020GC009375

Mendel, V., Sauter, D., Rommevaux-Jestin, C., Patriat, P., Lefebvre, F., & Parson, L. M. (2003). Magmato-tectonic cyclicity at the ultra-slow spreading Southwest Indian Ridge: Evidence from variations of axial volcanic ridge morphology and abyssal hills pattern. *Geochemistry, Geophysics, Geosystems*, *4*, 9102. https://doi.org/10.1029/2002GC000417

Momoh, E., Cannat, M., & Leroy, S. (2020). Internal structure of the oceanic lithosphere at a melt-starved ultraslow-spreading mid-ocean ridge: Insights from 2-D seismic data. *Geochemistry, Geophysics, Geosystems*, *21*. https://doi.org/10.1029/2019GC008540

Momoh, E., Cannat, M., Watremez, L., Leroy, S., & Singh, S. C. (2017). Quasi-3-D seismic reflection imaging and wide-angle velocity structure of nearly amagmatic oceanic lithosphere at the ultraslow-spreading Southwest Indian ridge. *Journal of Geophysical Research: Solid Earth*, *122*, 9511–9533. https://doi.org/10.1002/2017JB014754

Nicolas, A., Boudier, F., & France, L. (2009). Subsidence in magma chamber and the development of magmatic foliation in Oman ophiolite gabbros. *Earth and Planetary Science Letters*, *284*, 76–87. https://doi.org/10.1016/j.epsl.2009.04.012

Nicolas, A., Boudier, F., Koepke, J., France, L., Ildefonse, B., & Mevel, C. (2008). Root zone of the sheeted dike complex in the Oman ophiolite. *Geochemistry, Geophys. Geosystems*, *9*. https://doi.org/10.1029/2007GC001918

Olive, J.-A., & Crone, T. J. (2018). Smoke without fire: How long can thermal cracking sustain hydrothermal circulation in the absence of magmatic heat? *Journal of Geophysical Research: Solid Earth*, *123*, 4561–4581. https://doi.org/10.1029/2017JB014900

Parson, L. M., Murton, B. J., Searle, R. C., Booth, D., Evans, J., Field, P., et al. (1993). En echelon axial volcanic ridges at the Reykjanes ridge: A life cycle of volcanism and tectonics. *Earth and Planetary Science Letters*, *117*, 73–87. https://doi.org/10.1016/0012-821X(93)90118-S

Phipps Morgan, J., & Chen, Y. J. (1993). Dependence of ridge-axis morphology on magma supply and spreading rate. *Nature*, *364*, 706–708. https://doi.org/10.1038/364706a0

Pitzer, K. S., Peiper, J. C., & Busey, R. H. (1984). Thermodynamic properties of aqueous sodium chloride solutions. *Journal of Physical and Chemical Reference Data*, *13*, 1–102. https://doi.org/10.1063/1.555709

Sauter, D., Cannat, M., Rouméjon, S., Andreani, M., Birot, D., Bronner, A., et al. (2013). Continuous exhumation of mantle-derived rocks at the Southwest Indian Ridge for 11 million years. *Nature Geoscience*, *6*, 314–320. https://doi.org/10.1038/ngeo1771

Seher, T., Crawford, W. C., Singh, S. C., Cannat, M., Combier, V., & Dusunur, D. (2010). Crustal velocity structure of the Lucky Strike segment of the Mid-Atlantic Ridge at 37°n from seismic refraction measurements. *Journal of Geophysical Research: Solid Earth*, *115*. https://doi.org/10.1029/2009JB006650

Singh, S. C., Crawford, W. C., Carton, H., Seher, T., Combier, V., Cannat, M., et al. (2006). Discovery of a magma chamber and faults beneath a Mid-Atlantic Ridge hydrothermal field. *Nature*, *442*, 1029–1032. https://doi.org/10.1038/nature05105

Sinton, J. M., & Detrick, R. S. (1992). Mid-ocean ridge magma chambers. *Journal of Geophysical Research*, *97*, 197. https://doi.org/10.1029/91JB02508

Soule, S. A., Escartín, J., & Fornari, D. J. (2009). A record of eruption and intrusion at a fast spreading ridge axis: Axial summit trough of the East Pacific Rise at 9–10°N. *Geochemistry, Geophysics, Geosystems*, *10*. https://doi.org/10.1029/2008GC002354

Standish, J. J., Dick, H. J. B., Michael, P. J., Melson, W. G., & O'Hearn, T. (2008). MORB generation beneath the ultraslow spreading Southwest Indian Ridge (9-25°E): Major element chemistry and the importance of process versus source. *Geochemistry, Geophysics, Geosystems*, *9*(5). https://doi.org/10.1029/2008gc001959

Tao, C., Lin, J., Guo, S., Chen, Y. J., Wu, G., Han, X., et al. (2012). First active hydrothermal vents on an ultraslow-spreading center: Southwest Indian Ridge. *Geology*, *40*, 47–50. https://doi.org/10.1130/G32389.1

Tao, C., Seyfried, W. E., Lowell, R. P., Liu, Y., Liang, J., Guo, Z., et al. (2020). Deep high-temperature hydrothermal circulation in a detachment faulting system on the ultra-slow spreading ridge. *Nature Communications*, *11*, 1–9. https://doi.org/10.1038/s41467-020-15062-w

Theissen-Krah, S., Iyer, K., Rüpke, L. H., & Morgan, J. P. (2011). Coupled mechanical and hydrothermal modeling of crustal accretion at intermediate to fast spreading ridges. *Earth and Planetary Science Letters*, *311*, 275–286. https://doi.org/10.1016/j.epsl.2011.09.018

Wessel, P., Luis, J. F., Uieda, L., Scharroo, R., Wobbe, F., Smith, W. H. F., & Tian, D. (2019). The generic mapping tools version 6. *Geochemistry, Geophysics, Geosystems*, *20*, 5556–5564. https://doi.org/10.1029/2019GC008515

Wilcock, W. S. D., Hooft, E. E. E., Toomey, D. R., McGill, P. R., Barclay, A. H., Stakes, D. S., & Ramirez, T. M. (2009). The role of magma injection in localizing black-smoker activity. *Nature Geoscience*, *2*, 509–513. https://doi.org/10.1038/ngeo550

Yang, W., Tao, C., Li, H., Liang, J., Liao, S., Long, J., et al. (2017). 230Th/238U dating of hydrothermal sulfides from Duanqiao hydrothermal field, Southwest Indian Ridge. *Marine Geophysical Researches*, *38*, 71–83. https://doi.org/10.1007/s11001-016-9279-y

Yu, Z., Li, J., Niu, X., Rawlinson, N., Ruan, A., Wang, W., et al. (2018). Lithospheric structure and tectonic processes constrained by microearthquake activity at the Central ultraslow-spreading Southwest Indian ridge (49.2° to 50.8°E). *Journal of Geophysical Research: Solid Earth*, *123*, 6247–6262. https://doi.org/10.1029/2017JB015367

Zhao, M., Qiu, X., Li, J., Sauter, D., Ruan, A., Chen, J., et al. (2013). Three-dimensional seismic structure of the Dragon Flag oceanic core complex at the ultraslow spreading Southwest Indian Ridge (49°39′E). *Geochemistry, Geophysics, Geosystems*, *14*, 4544–4563. https://doi.org/10.1002/ggge.20264